1   Word Count: 8793

2   Revision 4

3 **Microchemistry and magnesium isotope composition of the Purang**

4 **ophiolitic chromitites (SW Tibet): New genetic inferences**

5 Fahui Xiong[1,2,*], Basem Zoheir[3,4], Paul T. Robinson[1], Richard Wirth[5], Xiangzhen Xu[1,2], Tian
6 Qiu[1,2], Yi Sun[6]

7

8 *[1]Center for Advanced Research on the Mantle (CARMA), Key Laboratory of Deep-Earth*
9 *Dynamics of Ministry of Land and Resources, Institute of Geology, Chinese Academy of*
10 *Geological Sciences, Beijing 100037, China*

11 *[2]Southern Marine Science and Engineering Guangdong Laboratory (Guangzhou)，511458,*
12 *China*

13 *[3]Department of Geology, Faculty of Science, Benha University, 13518 Benha, Egypt*

14 *[4]Institute of Geosciences, University of Kiel, Ludewig-Meyn Str. 10, 24118 Kiel, Germany*

15 *[5]Helmholtz Centre Potsdam, GFZ (German Research Centre for Geosciences), 3.5 Surface*
16 *Geochemistry, Germany*

17 *[6]School of Geosciences and Resources, China University of Geoscience (Beijing), Beijing*
18 *100083, China*

19

20

21 * *Corresponding author*: Dr. Fahui Xiong, 26 Baiwanzhuang Street, Beijing 100037, China;
22 Tel.: 86-15001105817; e-mail: xiongfahui@126.com

23   **ABSTRACT**

24   New petrographic and microanalytical studies of mineral inclusions in the Purang ophiolitic

25   chromitites (SW Tibet) are used to scrutinize the evolution of the associated Cretaceous

26   sub-oceanic lithospheric mantle section. Silicate inclusions in the chromite grains include

27   composite and single-phase orthopyroxene, clinopyroxene, amphibole, and uvarovite. Most

28   inclusions are sub-rounded or globular, whereas a few inclusions exhibit cubic/octahedral

29   crystal morphologies. The latter are randomly distributed in the large chromite grains, though

30   discrete aggregates are consistently confined to the grain centers. Abundant micron-scale,

31   clinopyroxene inclusions are topotaxially aligned along crystallographic planes. Less

32   abundant sulfide, wüstite, apatite and uvarovite inclusions are observed in some samples.

33   The trace element geochemistry of the Purang chromitite evoke parental MORB- and

34   boninite-like melts, consistent with the supra-subduction zone setting. The δ^{26}Mg values of

35   the high-Cr and high-Al chromitites range from -0.25 to -0.29‰ and -0.05 to -0.32‰,

36   respectively. The associated harzburgite has nearly overlapping δ^{26}Mg values of -0.13 to

37   -0.37‰, but pyroxenite sills show a rather wider range of the δ^{26}Mg values (-0.61 to -0.67‰).

38   The variable Mg isotope signatures, combined with abundant exotic, ultra-high pressure and

39   super reduced (UHP-SuR) mineral inclusions in the chromite grains, suggest that recycling

40   and recrystallization under different mantle conditions played an important role in the genesis

41   and evolution of these rocks. Further, discrete silicate, sulfide, and metal alloy inclusions in

42   the Purang chromitites are comparable to those reported in other Tethyan ophiolites, and

43   collectively suggest a common geodynamic evolution.

44

47

INTRODUCTION

49 The occurrence of ultra-high pressure (UHP) minerals, such as diamond, coesite and lamellar

50 exsolutions of clinopyroxene in chromitites from many ophiolitic belts has raised many

51 questions about processes operating in the formation of the oceanic lithosphere (e.g., Yang et

52 al. 2007, 2014; McGowan et al. 2015, Satsukawa et al. 2015, Su et al. 2015, Gong et al. 2016;

53 Xiong et al. 2018, 2019, 2020a). Micro-diamond occur as inclusions in ophiolitic chromitites,

54 with morphologies and carbon isotopic signatures dissimilar to diamonds in kimberlites and

55 high-grade metamorphic rocks (e.g., Liou and Tsujimori 2013; Griffin et al. 2016). Unlike

56 diamonds in other geological matrices and environments, the ophiolite-hosted

57 micro-diamonds (and moissanite) are commonly surrounded by amorphous carbon (a hard

58 solid glass, occasionally contains small chromite grains; Yang et al. 2014).

59 The paragenetic relationships of most ultra-high pressure and super-reduced (UHP-SuR)

60 mineral phases in ophiolites are largely unidentified. Results of numerous experimental

61 investigations indicate that the formation of diamonds and other UHP-SuR minerals in

62 ophiolites occurs at depths between 150 and 300 km (Yang et al. 2007; Yamamato et al. 2009;

63 Xiong et al. 2015). Also, peridotites with SuR-UHP mineral inclusions could have been

64 transported to the lithospheric mantle by passive upwelling (forced return flow), likely

65 induced by downward penetration and roll-back of a subducting lithospheric slab (e.g., Arai

66   2013; McGowan et al. 2015; Griffin et al. 2016), or related to a super-plume event (e.g.,

67   Maruayama et al. 2007; Liou and Tsujimori 2013; Xiong et al. 2015).

68   Magnesium isotopes have unique systematics in mantle and crustal materials, offering a

69   new approach for tracing crustal versus mantle source components in the arc magmas. Most

70   significant Mg isotope fractionation is related to low temperature geological processes,

71   whereas little fractionation occurs at high temperatures and pressures (Teng et al. 2007,

72   2010a,b). Consequently, large deviation from the well-constrained mantle Mg isotope

73   composition in a fresh (unweathered) mafic rock may be indicative of the nature and

74   magnitude of crustal input to the parental magma. Magnesium isotopic values in the arc

75   volcanic rocks (δ^{26}Mg $= -0.26\pm 0.07$) are generally heavier than those of mantle peridotites

76   (δ^{26}Mg $= -0.25 \pm 0.07$; Teng et al. 2010a). Such a deviation in the magnesium isotope

77   signature of these rocks has been attributed to contamination by isotopically heavy Mg in

78   subducting slabs in the mantle wedge (e.g., Li et al. 2017).

79   Studies of the Mg isotopic composition of mantle rocks can shed light on deep mantle

80   processes and in turn on the accretion history of the Earth (e.g., Wiechert and Halliday 2007).

81   Theoretical modeling indicates that the Mg isotope fractionation between spinel-group

82   minerals and silicates is dependent on the octahedral ion composition (B_2^{3+}) of the spinel

83   minerals (Young et al. 2015, Schauble 2011). According to Schauble (2011), inter-mineral

84   Mg isotope fractionations at 727°C (= 1000 K) are 0.6‰ for spinel ($MgAl_2O_4$), 0.2‰ for

85   magnesiochromite ($MgCr_2O_4$), and 0.1‰ for magnesioferrite ($MgFe_2O_4$). The Mg isotope

86   systematics can therefore be used to study the petrogenetic processes operating in the

87   formation of podiform chromitites (e.g., Dauphas et al. 2010; Teng et al. 2011; Su et al. 2015,

88   2021a; Xiao et al. 2016).

89   In the present study, the microtextural and compositional characteristics of the mineral

90   inclusions in the Purang chromitites are integrated with new magnesium isotope data of these

4

91   chromitites and the associated peridotites. The data can place constraints on the mantle

92   processes involved in the formation of the studied ophiolite and analogous podiform

93   chromitites in accretionary belts.

GEOLOGICAL SETTING

95   The Purang ophiolite is the largest mafic-ultramafic massif (~600 km^2) along the western

96   Yarlung Zangbo Suture Zone (YZSZ) in the southern Tibet (Fig. 1). The ultramafic rocks

97   include lherzolite, harzburgite, and subordinate dunite (Su et al. 2019; Xiong et al. 2018, 2019,

98   2020b). Most of the dunite bodies contain irregular masses of deformed chromitites (Fig. 1b).

99   In places, chromitite lenses are 2 to 10 m long and 0.5 to 6 m wide, consistently aligned in a

100   NW-SE direction conformable to the penetrative shear foliation in the host rocks. These

101   lenses are commonly associated with harzburgite, and are surrounded by 5 m thick dunite

102   envelopes (Fig. 2). These chromitite bodies have sharp contacts against dunite, whereas

103   contacts between dunite and harzburgite are obscured or irregular. In the dunite blocks,

104   Cr-spinel grains occur discretely and as disseminations and as inclusions in olivine. The

105   ultramafic section contains rare ophicalcite and is cut by dikes and sills of pyroxenite, dolerite,

106   gabbronorite and basalt (Fig. 1b). The Purang ophiolitic rocks are embedded in a Late

107   Cretaceous mélange of carbonate, shales, and volcanic rocks (Xiong et al. 2013; Liu et al.

108   2011; Fig. 1b).

109   A sequence of basalt, limestone, silty shale and chert overlies the Purang ophiolite rocks

110   (Liu et al. 2015). Fossil Radiolaria in the chert bands indicate an Upper Jurassic-Lower

111   Cretaceous age for these rocks (Huang et al. 2006). In the Purang ophiolite, basalts with

112   mixed enriched-MORB and OIB geochemical affinities were dated at ~137 Ma (Liu et al.

113   2015). Zircons from crosscutting doleritic and gabbroic dikes have U-Pb ages of 144 - 120

114 Ma (Xiong et al. 2020b; Liu et al. 2011), suggesting formation prior to the Early Cretaceous.

115 Peridotites from the Purang ophiolite yielded nearly constant $\varepsilon_{Nd(t)}$ values of +6.1 to +6.2, and

116 $(^{86}Sr/^{87}Sr)_t$ values of 0.70688–0.70710 (Xiong et al. 2020b).

117   The occurrence of UHP-SuR mineral inclusions in the Purang chromitites was first

118 reported by Yang et al. (2015). In another example of the Tibetan chromitites, Yamamoto et

119 al. (2009) suggested that acicular clinopyroxene inclusions in chromite grains from the

120 Luobusa chromitite were formed under ultra-high pressure (UHP) conditions. Also, the $\delta^{13}C$

121 and $\delta^{15}N$ signatures of microdiamonds recovered from Luobusa chromitites and peridotites

122 suggest formation near the mantle transition zone (MTZ) (Xu et al. 2018).

123   **ANALYTICAL METHODS**

124   For the present study, 68 samples of the Purang chromitites were collected from ten

125 separate ore bodies (Fig. 1b). The mineral chemistry of chromite grains and silicate inclusions

126 were obtained using a JEOL JXA-8100 electron probe micro-analyzer (EPMA) at the Key

127 Laboratory of Deep-Earth Dynamics of Ministry of Natural Resources (Beijing). This EPMA

128 is equipped with three wavelength-dispersive spectrometers and an energy-dispersive Oxford

129 EDX spectrometer. The measuring conditions were 15 kV accelerating voltage, 20 nA beam

130 current, and 2 μm beam diameter. The EPMA data of the studied rocks are given in Tables

131 1-2. Routine quantification to 1% reproducibility was obtained over the many analysis

132 sessions, whereas accuracy remained ~ 1-2 % for the major elements.

133   The Raman spectra were collected by using a Horiba LabRAM HR Evolution

134 spectrometer at the Institute of Geology, Chinese Academy of Geological Sciences. This

135 spectrometer is equipped with an Olympus BX41 optical microscope. The room temperature

136 of 23 ± 1 °C was maintained during measurements, and a 532 nm air-cooled frequency double

137 Nd: YAG laser was employed under laser power of 80 mW. The scattered light was directed

138 to the spectrograph through a confocal 100 μm pinhole and then was received by a 1800

139 gr/mm diffraction grating. A CCD camera (Syncerity) was consistently cooled to -60 °C

140 while collecting the scattered light. Raman signals were collected for the spectral interval of

141 100–600 cm^{-1} with a spectral resolution of <0.6 cm^{-1} and calibrated with a silicon wafer peak

142 at 520.7 cm^{-1}. The acquisition of the Raman spectra comprised 2 accumulations of 1 s each.

143 Raman shifts were further calibrated with a plane (0001)-parallel section of euhedral

144 pegmatitic α-quartz. The latter showed main Raman peaks at 128, 206, and 464 cm^{-1} (average

145 of 85 standard measurements) during the measuring session.

146 Trace element compositions of chromite grains were obtained by using a laser ablation

147 system with an Agilent 7700x ICP-MS at the State Key Laboratory of Ore Deposit

148 Geochemistry, IGCAS. Laser sampling was performed using a GeoLas Pro 193 nm ArF

149 excimer laser. Argon (900 mL/min) was the make-up gas mixed with the carrier gas, helium

150 (580 mL/min), via a Y-connector before entering the ICP. The spot size was either 60 or 90

151 μm, depending on the size of the analyzed grains.

152 Transmission electron microscopy (TEM) micro-foils (15×10×0.20 μm) were prepared

153 using the focused ion beam (FIB) technique (Wirth 2009). A single focused ion beam device

154 (FEI-FIB 200 TEM) at the GFZ Potsdam was used for sample preparation. A Ga-ion beam

155 was applied to protect the surface of the sample and to extract foils (see Wirth 2009). A

7

156   TECNAI F20 XTWIN model TEM equipped with a Gatan Tridiem™ energy filter, an EDAX

157   Genesis™ X-ray analyzer and a Fishione high angle annular dark field detector (HAADF)

158   were used to study the mineral inclusions. A field emission gun (FEG) was used as the

159   electron source and the applied measuring conditions were 200 kV (Wirth et al. 2009).

160   Fresh representative samples were used for whole-rock Mg isotope analyses. The selected

161   rock samples were crushed in a corundum jaw crusher to 60 mesh, from which ~60 g of each

162   sample was pulverized in an agate ring mill to < 200 mesh. Sample preparation and chemical

163   digestion were carried out in a clean lab environment. Sample powders were weighted and

164   dissolved in a mixture of ultra-pure concentrated acids $HF-HNO_3$ (~3:1) in Savillex screw-cap

165   beakers. Sealed beakers were placed on a hot plate to 160°C for 24 hrs. The solutions were

166   then evaporated to dryness, dissolved in aqua regia, and heated to 130°C overnight. On the

167   following day, solutions in aqua regia were evaporated to dryness and refluxed with ultrapure

168   concentrated HNO_3 to ensure complete solution. The repeatedly evaporated concentrates

169   yielded a dried residue which was dissolved in 1 N HNO_3 for chromatographic separation.

170   Magnesium isotope compositions of the studied samples were measured by a Neptune

171   MC-ICP-MS at China University of Geosciences (Beijing), following the procedures

172   described in Teng et al. (2010b). The isotopic values were measured by the sample-standard

173   bracketing method in the low-resolution mode. The in-run precision on the $^{26}Mg/^{24}Mg$ ratio

174   for a single block of 40 measurements was less than ± 0.02‰ (2SD). The USGS standard

175   BHVO-2 gave acceptable $\delta^{26}Mg$ values of −0.27 ± 0.04‰ in the measurement session (e.g.,

176   Huang et al. 2015).

177

RESULTS

Chromitite bodies and Cr-spinel grains in the Purang peridotites

Irregular chromitite lenses and less common amoeboid chromite patches characterize

peridotites of the Purang ophiolite (Xiong et al. 2018). In harzburgite, Cr-spinel grains have

variable Cr# and Mg# values of 26.1-44.7 and 54.1-66.6, respectively (Fig. 3). Disseminated

Cr-spinel grains in dunite samples have less variable and consistently higher Cr# (~45.9-69.9)

and Mg# (49.5-61.8) values (Table 1). In the chromitite masses, Cr-spinel grains have Cr#

values of 47.6 - 58.4 and Mg# values of 53.2 - 75.8, classifying them as high-Al chromite

(e.g., Melcher et al. 1997; Zhou and Robinson 1997). Also present are Cr-spinel grains with

Cr# values of 63.8 to 88.5 and Mg# values of 45.9 - 74.8, typical of high-Cr chromite (Table

1).

189

Mineral inclusions in chromite

We identified distinct groups of inclusions in the chromite grains from the Purang chromitite.

Discrete globular to anhedral inclusions are composed of pyroxene (Figs. 4, 5, 6).

Submicroscopic (~1 μm-thick) acicular silicate inclusions (Fig. 4) seem to be controlled by

specific crystallographic planes (e.g., Yamamoto et al. 2009). Although inclusions in the

different thin sections are variable in abundance and relative proportions, the two chromite

types, high-Cr and high-Al, show no distinct variations in the inclusion types (see

Supplementary Material 1).

9

198   Also observed are euhedral orthopyroxene inclusions (5-20 μm diameter) that exhibit

199   octahedral habits (Figs. 5a - 5c). Other small subhedral to euhedral inclusions (5 - 15 μm)

200   with triangular forms are mainly clinopyroxene (Figs. 5d - 5f). Most of the subhedral

201   inclusions show octahedral morphologies (Fig. 5), and are characterized by ubiquitous

202   interface angles of 54-68° (Figs. 4, 5). Sparse acicular silicate inclusions are arrayed

203   subparallel, though few of them appear to be randomly oriented. The X-ray elemental

204   mapping and EDX of some acicular inclusions show two main peaks, Si and Ca (Figs. 6d),

205   with no apparent Al, Cr and Fe spectra (Figs. 6d; Supplementary Material 2). The abundances

206   of Mg and O are very low (Supplementary Material 2) and some of these acicular inclusions

207   show chemical zoning as indicated by the EDS and WDS results. The Raman spectra

208   collected for these inclusions show scattered peaks superposed on a broad diffuse scattering

209   pattern (Supplementary Material 3). These mixed or composite spectra identify bands with

210   definite M-O stretching at ~322 cm^{-1}, Mg-O stretching at ~388 cm^{-1}, Si-O-Si bending at ~665

211   cm^{-1}, and Si-O stretching at ~1012 cm^{-1} (Supplementary Material 3, Huang et al. 2000).

212   Orientation along specific crystallographic planes and the topotaxial relationship are

213   emphasized by the TEM images of some large chromite grains (Fig. 6). The average

214   composition of many of these inclusions can be formulated as $En_{52.0}Fs_{1.5}Wo_{46.4}$ (Table 2). On

215   the other hand, orthopyroxene inclusions are mainly enstatite with high Mg# values of ~ 96.4

216   to 96.8, and nearly constant Al_2O_3 contents (0.28-0.36 wt.%; Table 2). Moreover, scattered

217   amphibole inclusions exhibit irregular morphologies along or adjacent to micro-fissures in the

218   high-Al chromite grains (Supplementary Material 4). Amphibole inclusions form small

219 subhedral crystals (Figs. 7), commonly associated with phlogopite, apatite, orthopyroxene,

220 and clinopyroxene in composite inclusions.

221 Discrete base metal mineral inclusions, including sulfides and Fe±Co±Ni±As alloys,

222 were observed in some chromite grains. These inclusions vary significantly in size (from few

223 microns to several hundreds of microns) and exhibit irregular or globular morphologies (Fig.

224 8). Base metal sulfides are commonly associated with metal alloy inclusions. Small, blocky

225 inclusions of pentlandite (Fig. 8f) and a ~ 5 μm-long triangular inclusion of wüstite (FeO)

226 were observed in a single sample (Supplementary Material 5).

227 Dispersed Ni–Cu–Fe (Co) sulfides in the Purang chromitite occur as discrete particles or

228 as inclusions in the chromite grains. Uncommon metal alloys include Ni-Fe, Ni-Cu-Fe, Fe-Co,

229 and Ni-As grains, varying in size from 5 to 200 μm. We observed more abundant Ni-Fe alloy

230 inclusions in the high-Cr chromite than in the high-Al chromite. A single inclusion of an

231 Fe-Co alloy was observed next to a microfracture in a large chromite grain (Fig. 8). Metal

232 alloy inclusions with variable compositions are associated with goethite along microfractures

233 (Fig. 8). In addition, dispersed minute inclusions of Os-Ir-Fe-Ni alloys are intergrown with

234 silicate phases (Supplementary Material 6).

235 The TEM image of an acicular inclusion (50 μm × 2μm, Fig. 9a) shows bright zones

236 surrounded by a darker domain. Line mapping shows that these bright zones are rich in Si, Fe,

237 O and poor in Al and Mg (Fig. 9b). Another unusual inclusion is the irregular mass of apatite

238 that occupies interstices between chromite grains or perhaps microcracks (Fig. 7b). An

239 irregular grain ~120 μm × ~ 30 μm consists of Ca phosphate and Ti (Fig. 10).

11

240   An inclusion of uvarovite (20 μm × 100 μm) has sharp but irregular contacts with the host

241   chromite grain (Fg. 7c), though its contact appears to be gradational in the TEM image (Fig.

242   10a). The EDX spectrum of this uvarovite inclusion shows prominent peaks for Ca, Si, Al, Cr

243   and O and minor peaks for Fe and Ti. The indexed diffraction pattern (Fast Fourier Transform,

244   FFT) of this inclusion (Fig. 10a) validates its isometric structure.

245   **Minor and trace elements in chromite and Cr-spinel grains**

246   In situ minor and trace element concentration of chromite grains are shown in Table 3. The

247   high-Al chromite grains have Ga contents of 37-61 ppm, 652-2272 ppm Ni, and 186-318 ppm

248   Co, whereas high-Cr chromite has lower Ga (30–41 ppm), Ni (871-1694 ppm) and Co

249   (187-243 ppm) contents. Both the high-Cr and high-Al chromite varieties have similar

250   concentrations of Ti (457-1499 ppm vs 435-1161 ppm), V (777-995 ppm vs 661-1227 ppm),

251   Mn (1043-1348 ppm vs 900-1730 ppm), and Zn (371-571 ppm vs 400-776 ppm) (Table 3).

252   The high-Al and high-Cr chromite varieties show largely overlapping contents of Sc, V, Mn,

253   Zn, and Zr. Within each group, there is a modest positive correlation between Cr# and Sc. The

254   overall data set shows negative correlation between Cr# and both Ga and Ni (Fig. 11). The

255   MORB-normalized trace element patterns of both chromite varieties are similar and show

256   variable depletions in Ga, Ti, and Ni, and relative enrichments in Zn, Co, Mn and V. Most

257   patterns are characterized by depletion in Sc, but some grains are mildly enriched in Sc (Fig.

258   12). Generally, chromite grains from the Purang chromitites show fractionated transition

259   metal compositions, consistent with crystallization from a depleted mantle source. The trace

260   element patterns of the analyzed chromite varieties partially overlap the typical patterns of

261   Cr-spinel from boninites (BON) and high-Cr chromitites of the Ordovician Thetford Mines

12

262   Ophiolite (RMO; Pagé and Barnes 2009). The latter is interpreted as a fragment of fore-arc

263   oceanic lithosphere (Pagé and Barnes 2009).

264   Cr-spinel grains disseminated in the lherzolite and harzburgite members of the Purang

265   ophiolite have similar trace element contents, with variable contents of Ga (16.1-40.2 ppm),

266   Ni (233-1466 ppm), and Co (147-439 ppm) (Su et al. 2019). The Cr-spinel grains in the dunite

267   samples have similar Cu, Zn, Ca, Rb and Ga contents, but relatively depleted Ti, Co, Nb and

268   Zr.

269   **Magnesium isotopic compositions of the Purang ophiolitic rocks**

270   The Mg isotopic compositions of selected fresh samples from the Purang chromitites and

271   peridotites are given in Table 4. The δ^{26}Mg values of five high-Al chromite-dominated

272   chromitites range between -0.32 to -0.05 ‰ ±0.04 ‰. Three high-Cr chromite-dominated

273   chromitite samples yield overlapping δ^{26}Mg values of -0.29 to -0.25 ‰ ±0.04‰. Three

274   harzburgite samples show variable δ^{26}Mg values of -0.37 ‰ ±0.04 ‰ to -0.13 ±0.02‰, and

275   two pyroxenite samples have noticeably light values of -0.67 and -0.61 ‰ ±0.05 ‰ (Table 4,

276   Fig. 13). The Mg isotope values of the analyzed samples are distinctively variable for the

277   high-Al chromitite variety compared to the nearly constant values of the high-Cr chromitite

278   and peridotites. The Mg isotopic compositions of the host peridotites are much lighter than

279   those of high-Cr and high-Al chromitites.

280

281 **DISCUSSION**

282 **Mineralogical and geochemical characteristics**

283 Olivine, orthopyroxene, and clinopyroxene inclusions in ophiolitic chromite grains are

284 commonly interpreted as captive mineral phases (e.g., Zhou et al. 2014). In the chromite

285 grains from the Purang chromitites, silicate inclusions have Mg# values and Cr_2O_3 and TiO_2

286 contents distinctive from those of olivine and pyroxene in the host peridotites (Fig. 3). The

287 morphology and distribution of these mineral inclusions clearly suggest an early paragenesis

288 (Fig. 5). According to González-Jiménez et al. (2014), island arc basaltic magmas can react

289 with other silicate melts or mantle peridotites, leading to an increase in the SiO_2 content to

290 promote chromite grain crystallization. In the mantle peridotite-melt reaction, pyroxene

291 dissolves into the melt and causes variable enrichment in several incompatible elements,

292 including the rare earth elements (REE).

293 The plagioclase, zircon, rutile, amphibole, calcite, apatite and phlogopite inclusions show

294 mostly sharp contact relationships with the host minerals (Figs. 7, 10). Crystallization of such

295 inclusions may be triggered by late fluid circulation in the subduction zone (Zaeimnia et al.

296 2017; Johan et al. 2017; Xiong et al. 2018). The rutile and ilmenite inclusions in the chromite

297 grains can be explained by post-formation high-grade metamorphism of their host rocks. In

298 the subduction zone environment, basaltic melts may alter chromian spinel, and then rutile,

299 ilmenite, and titanite are enclosed during the newly crystallized chromite (Qiu et al. 2021).

300 The trace compositions of the high-Al and high-Cr chromite varieties from the Purang

301 ophiolite are comparable to the Luobusa chromitite (Su et al. 2019). The decreasing trends of

302 compatible elements, such as Ni and Ga, in chromite with Cr# suggest that these elements

303 were controlled by both partial melting and melt diffusion (Fig. 11; Su et al. 2019). The

304 correlation between Zr, V and Sc contents in chromite and Cr# values may suggest diffusion

305 of these elements into melts during melt-rock interaction (Fig. 11). The parental magmas of

306 the Purang dunites and chromitites are suggested to have been intermediate in composition

307 between boninitic and MORB-like melts (Fig. 3). Recycling of both oceanic and continental

308 crustal minerals has been considered as a model of formation of the Luobusa chromitites and

309 peridotites (Zhou et al. 2014; Shi et al. 2007; Yang et al. 2007, 2015; Yamamoto et al. 2009;

310 Wang et al. 2021). Such recycling process is compatible with the high contents of Nb, Zr and

311 Ti in chromitites, as these elements are enriched in the crustal materials. The Sc depletion in

312 the Purang chromitites may be explained by diffusion during melt-rock reaction (Spandler et

313 al. 2007; Pagé and Barnes 2009).

314 Base Metal Sulfide (BMS) and platinum-group element (PGE) mineral inclusions are

315 abundant in chromite grains from the Purang podiform chromitites (Fig. 8). These inclusions

316 are dominated by Ru-rich alloys (Supplementary Material 6; Xiong et al. 2018). According to

317 Prichard et al. (2008), saturation of the PGE is proportional to the extent of reaction between

318 PGE minerals and the melt during chromite formation. This results in PGE minerals

319 (including Ni–Cu–Fe sulfides and PGE alloys) forming micron- to millimeter-scale inclusions

320 in peridotites (e.g., Marchesi et al. 2011; Akmaz et al. 2014). A rise in sulfur fugacity during

321 magma cooling, causes heazlewoodite to transform into millerite and the PGE alloys to

322 dissolve (González-Jiménez et al. 2012), and hence some PGE-rich inclusions could have

323 formed during the recrystallization of chromitites.

324 According to Brenan and Andrews (2001) and Andrews and Brenan (2002), the

325 abundance of Os-bearing laurite indicates high sulfur fugacity values ($log fS_2$ = -2 to -1.3) and

326 temperatures not exceeding 1200°C during chromite crystallization. Microdiamond,

327 moissanite, pseudomorphic octahedral silicates and crustal mineral inclusions (e.g., rutile,

15

328   monazite, zircon, etc.) have been reported in the Purang lherzolite (Xiong et al. 2019). Also,

329   Yang et al. (2015) described scarce UHP minerals in the Luobusa and Ray-Iz chromitites.

330   The lower-pressure isometric structure chromite phase forms as a consequence of

331   decompression and breakdown of an original high-pressure Ca-ferrite structure chromite

332   phase (CF-type). Griffin et al. (2016) suggested that clinopyroxene and the HP silica

333   polymorph (coesite) develop due to the insoluble nature of Ca and Si in isometric chromite

334   (Figs. 4, 6). The clinopyroxene-chromite association indicates their common paragenesis (Su

335   et al. 2019; Liu et al. 2020). In the Purang lherzolites, Gong et al. (2016) interpreted the

336   clinopyroxene-chromite association to represent symplectites that developed by the

337   breakdown of garnet under the spinel peridotite stability field. Arai (2013) suggested that

338   chromite will revert to the original isometric structure and olivine assemblage during

339   recycling of mantle UHP to low-pressure magmatic conditions. These inclusions may

340   preserve partially obliterated orbicular textures (Fig. 4). The UHP Ca-ferrite type chromite

341   with diamond and other carbon-bearing UHP mineral inclusions can be derived from

342   methane-rich fluid species (Figs. 4 and 6; Yang et al. 2007; Arai 2013). Exsolution lamellae

343   of silica and clinopyroxene may also develop at depths above the mantle transition zone

344   (Yamamoto et al. 2009). The Purang lherzolitic peridotites are interpreted as residues of 10–

345   15% partial melting of a fertile mantle source in a seafloor spreading setting (Xiong et al.

346   2018). Both orthopyroxene and clinopyroxene porphyroclasts in these lherzolites form

347   exsolution lamellae, which can be explained by upwelling of these rocks into shallow mantle

348   depths and associated crystal–plastic deformation (Xiong et al. 2020c). In the Purang

349   chromite, olivine, clinopyroxene and orthopyroxene could have crystallized from anhydrous

350   melts, whereas amphiboles and phlogopite could have formed from water-rich melts (Fig. 7).

351   The conditions estimated for the formation of the Purang lherzolites are 700-1000°C and

352   1.3-2.3 GPa, which correspond to mantle depths of ~100 km (Xiong et al. 2020c). These

353   temperature-pressure estimates are thought to represent the lower limit of conditions under

354   which decomposition of pyroxenes takes place.

355   **Evolution of the Purang ophiolite**

356   Pyroxenes in the Purang lherzolites have compositions typical of pyroxenes in abyssal

357   peridotites (e.g., Xiong et al. 2013, 2020c). The low Cr# values (~25-30) and TiO_2 contents ($\leq$

358   0.1 wt. %) in disseminated Cr-spinel from the Purang lherzolites suggest 10-15% melting of a

359   N-MORB–type mantle source (Hellebrand et al. 2001). The clinopyroxene inclusions and

360   blebs in orthopyroxene porphyroclasts in Purang lherzolite suggest direct crystallization from

361   infiltrating/stagnant melts or interaction of metasomatized melts with residual peridotites

362   (e.g., Suhr et al. 1998; Seyler et al. 2007). For the Purang peridotites, measured $^{187}Os/^{188}Os$

363   ratios (0.12289 - 0.13194; Gong et al. 2016) are within the range of those reported for other

364   mantle-hosted podiform chromitites (Xiong et al. 2018). In addition, the generally low γOs

365   values (< 1) of chromitites indicate that their parental melts were sourced from a

366   heterogeneously depleted mantle region above a downgoing lithospheric slab (e.g., Xiong et

367   al. 2018).

368   Water in the podiform chromitites hydrates surrounding silicate minerals in the chromitite

369   and/or penetrates the surrounding wall rocks (Matveev and Ballhaus 2002; Boudreau et al.

370   2010; Su et al. 2020). Uvarovite (Fig. 11) could have crystallized from a metasomatized

371   MORB-like melt that likely infiltrated deformed chromite grains (e.g., Su et al. 2019).

372   Partial melting occurred at the mid-ocean ridge stage and generated oceanic mafic crust

373   with low $\delta^{26}Mg$ values, leaving refractory peridotites with isotopically heavy Mg behind (Su

17

374   et al. 2015, 2021a). The variations of Mg isotopic compositions of the Purang peridotites can

375   be interpreted as a feature of multi-stage melting and metasomatism of the oceanic

376   lithospheric mantle (Fig. 13: Su et al. 2015). Dolerite and gabbro complexes from the Purang

377   ophiolite gave zircon U–Pb ages ranging from 144.2 ±2.1 Ma to 126.5 ±0.4 Ma and generally

378   positive zircon $\varepsilon_{Hf(t)}$ values, suggesting a heterogenous juvenile mantle source (Liu et al. 2011;

379   Xiong et al. 2020b).

380   Oceanic basalts and peridotites commonly show identical δ^{26}Mg values since

381   high-temperature mantle processes do not efficiently fractionate Mg isotopes (e.g., Bourdon et

382   al. 2010; Pogge von Strandmann et al. 2011). In the Purang ophiolite, the average δ^{26}Mg of

383   peridotites (-0.20 ± 0.10 ‰) is slightly higher than both chondrites and oceanic basalts values

384   (Su et al. 2019). Also, the δ^{26}Mg values of the Purang ophiolitic rocks do not correlate with

385   common indices for partial melting and metasomatism (Supplementary Material 7; Su et al.

386   2019). In the Luobusa and Zedong harzburgites, the similar δ^{26}Mg values (-0.41 to -0.20‰)

387   for olivine, orthopyroxene and chromite concentrates have been interpreted to reflect an

388   equilibrium isotope fractionation (Xiao et al. 2016). In the Purang ophiolite, the high-Cr and

389   high-Al chromitites have Mg isotopic compositions slightly lighter than those of the

390   associated peridotites (Fig. 13; Supplementary Material 7). In peridotite xenoliths, olivine

391   with negative Mg–Fe isotopic values has likely experienced Fe–Mg inter-diffusion with

392   metasomatic melts in sub-arc mantle environments (Huang et al. 2011; Sio et al. 2013; Zhou

393   et al. 2014).

394

IMPLICATIONS

395

396   The chemical characteristics of the Purang ophiolitic chromitites, including trace element

397   patterns and Mg isotope composition, are comparable to chromitites formed in a fore-arc SSZ

398   setting. Formation of the Purang ophiolites in a SSZ setting is corroborated by the occurrence

399   of basaltic component with mixed enriched-MORB and OIB geochemical affinities.

400   Inclusions of uvarovite, apatite, lamellar clinopyroxene and wüstite in the Purang chromitite

401   may reflect fluid percolation in the lithospheric mantle. Considering the abundant UHP and

402   SuR mineral inclusions in the investigated chromitites, the Purang ophiolite likely

403   experienced a complex petrogenetic history encompassing deep mantle processes. Mantle

404   convection may have transported chromitites and the associated peridotites to shallow mantle

405   levels, leading to partial melting of peridotites, recrystallization of chromitites and

406   encapsulation of crustal and exotic silicates, sulfides, and metal alloys as inclusions.

407   This study reports Mg isotope compositions of Purang ophiolite comparable to other

408   Tethyan ophiolites, implying a common geodynamic evolution. As a part of the Neo-Tethyan

409   ophiolites, the Purang podiform chromitites record superimposed deep mantle and

410   subduction-related processes. Partial hydrous melting of the mantle wedge could have

411   produced island arc tholeiitic and boninitic magmas that reacted with peridotites and endowed

412   parts of this mantle section with chromite ores.

413

19

ACKNOWLEDGMENTS

428   **REFERENCES**

429   Akmaz, R.M., Uysal, I., and Saka, S. (2014) Compositional variations of chromitite and solid

430   inclusions in ophiolitic chromitites from the southeastern Turkey: Implications for

431   chromitite genesis. Ore Geology Reviews, 58, 208-224.

432   Arai, S. (2013) Conversion of low-pressure chromitites to ultrahigh-pressure chromitites by

433   deep recycling: a good inference. Earth & Planetary Science Letters, 379, 81-87.

434   Arai., S. (1997). Control of wall-rock composition on the formation of podiform chromitites

435   as a result of magma/peridotite interaction. Resource Geology, 47, 177-187.

20

436 Andrews, D.R.A. and Brenan, J.M. (2002) Phase-equilibrium constraints on the magmatic

437   origin of laurite + Ru-Os-Ir alloy. Canadian Mineralogist, 40, 1705–1716.

438 Barnes, S.J., Naldrett, A.J., and Gorton, M.P. (1985) The origin of the fractionation of the

439   platinum-group elements in terrestrial magmas. Chemical Geology, 53, 303–323.

440 Brenan, J.M. and Andrews, D. (2001) High-temperature stability of laurite and Ru–Os–Ir

441   alloy and their role in PGE fractionation in mafic magmas. Canadian Mineralogist, 39,

442   341–360.

443 Bourdon, B., Tipper, E.T., Fitoussi, C. and Stracke, A. (2010) Chondritic Mg isotope

444   composition of the Earth. Geochimica Et Cosmochimica Acta, 74, 5069–5083.

445 Dauphas, N., Teng, F.Z. and Arndt, N.T. (2010) Magnesium and iron isotopes in 2.7 Ga

446   Alexo komatiites: Mantle signatures, no evidence for Soret diffusion, and identification

447   of diffusive transport in zoned olivine. Geochimica Et Cosmochimica Acta, 74, 3274–

448   3291.

449 Dick, H.J. and Bullen, T. (1984) Chromian spinel as a petrogenetic indicator in abyssal and

450   alpine-type peridotites and spatially associated lavas. Contributions to Mineralogy and

451   Petrology, 86, 54–76.

452 González-Jiménez, J.M., Griffin, W.L., Gervilla, F., Proenza, J.A., O'Reilly, S.Y. and

453   Pearson, N.J. (2014) Chromitites in ophiolites: how, where, when, why?, Part 1. A

454   review and new ideas on the origin and significance of platinum-group minerals. Lithos,

455   189, 127–139.

456 González-Jiménez, J.M., Griffin, W.L., Gervilla, F., Kerestedjian, T.N., O'Reilly, S.Y.,

457   Proenza, J.A., Pearson, N.J. and Sergeeva, I. (2012) Metamorphism disturbs the Re-Os

458   signatures of platinum-group minerals in ophiolite chromitites. Geology, 40, 659–662.

459 Gong, X.H., Shi, R.D., Griffin, W.L., Huang, Q.S., Xiong, Q., Chen, S.S., Zhang, M., and

460   O'Reilly, S.Y. (2016) Recycling of ancient subduction-modified mantle domains in the

461   Purang ophiolite (southwestern Tibet). Lithos, 262, 11–26.

462 Griffin, W.L., Afonso, J.C., Belousova, E.A., Gain, S.E., Gong, X.-H., González-Jiménez,

463   J.M., Howell, D., Huang, J.-X., McGowan, N., Pearson, N.J., Satsukawa, T., Shi, R.,

464   Williams, P., Xiong, Q., Yang, J.-S., Zhang, M. and O'Reilly, S.Y. (2016) Mantle

21

465   recycling: Transition Zone metamorphism of Tibetan ophiolitic peridotites and its

466   tectonic implications. Journal of Petrology, 1–30.

467 Hébert, R., Huot, F., Wang, C.S. and Liu, Z.F. (2003) Yarlung Zangbo ophiolites (southern

468   Tibet) revisited: geodynamic implication from the mineral record. In: Dilek, Y.,

469   Robinson, P.T. (Eds.), Ophiolites in Earth History. Geological Society London Special

470   Publications, 165–190.

471 Hellebrand, E., Snow, J.E., Dick, H.J.B. and Hofmann, A.W. (2001) Coupled major and trace

472   elements as indicators of the extent of melting in mid-ocean-ridge peridotites. Nature,

473   410, 677–681.

474 Ishii, T., Robinson, P.T., Maekawa, H., and Fiske, R. (1992) Petrological studies of peridotites

475   from diapiric serpentinite seamounts in the Izu-Ogasawara-Mariana forearc, Leg 125

476   Proceedings of the Ocean Drilling Program, Scientific Results, 125, 445–485.

477 Huang, E., Chen, C.H., Huang, T., Lin, E.H. and Xu, J. (2000) Raman spectroscopic

478   characteristics of Mg-Fe-Ca pyroxenes. American Mineralogist, 85,473–479.

479 Huang, G.C., Mo, X.X., Xu, D.M., Lei, Y.J. and Li, L.J. (2006) Origination and evolution of

480   Daba-Xiugugabu ophiolite belt in the Southwestern Tibet. Geology and Mineral

481   Resources of South China, 3, 1–9 (in Chinese with English abstract).

482 Huang, F., Zhang, Z.F., Lundstrom, C.C. and Zhi, X.C. (2011) Iron and magnesium isotope

483   compositions of peridotite xenoliths from Eastern China. Geochimica Et Cosmochimica

484   Acta, 75, 3318–3334

485 Huang, J., Li, S.G., Xiao, Y.L., Ke, S., Li, W.Y. and Tian, Y. (2015) Origin of low δ^{26}Mg

486   Cenozoic basalts from South China Block and their geodynamic implications.

487   Geochimica Et Cosmochimica Acta, 164, 298–317.

488 Huang, M.X., Yang, J.J., Powell, R. and Mo, X.X. (2014) High-pressure metamorphism of

489   serpentinizedChromitite at Luobusa (souther Tibet). American Journal of Science, 314:

490   400–433.

491 Johan, Z., Martin, R.F. and Ettler, V. (2017) Fluids are bound to be involved in the formation

492   of ophiolitic chromite deposits. European Journal of Mineralogy, 29, 543–555

493   Li, S.-G.,   Yang, W., Ke,   S., Meng, X.-N., Tian, H.-C.,   Xu, L.-J.,   He, Y.-S.,   Huang, J.,
494   Wang, X.-C., Xia, Q.-K., Sun, W.-D., Yang, X.-Y., Ren, Z.-Y., Wei, H.-Q., Liu, Y.-S.,
495   Meng, F.-C., and Yan, J. (2017) Deep carbon cycles constrained by a large-scale mantle
496   Mg isotope anomaly in eastern China. National Science Review, 4, 111-120

497   Liou, J.G. and Tsujimori, T. (2013) The fate of subducted continental crust: Evidence from
498   recycled UHP-UHT minerals. Elements, 9, 248–250.

499   Liu, F., Yang, J.S., Dilek, Y., Xu, Z.Q., Xu, X.Z., Liang, F.H., Chen, S.Y. and Liang, D.Y.
500   (2015) Geochronology and geochemistry of basaltic lavas in the Dongbo and Purang
501   ophiolites   of   the   Yarlung-Zangbo   Suture   zone: plume-influenced   continental
502   margin-type oceanic lithosphere in southern Tibet. Gondwana Research, 27, 701–718.

503   Liu, Z., Li, Y., Xiong, F.H., Wu, D. and Liu, F. (2011) Petrology and geochronology of MOR
504   gabbro in the Purang ophiolite of western Tibet, China. Acta Petrolica Sinica in Chinese,
505   27, 3269–3279.

506   Liu, X., Su, B. X., Bai, Y., Robinson, P. T., Tang, X., Xiao, Y., Xue, D. S. And Cui, M. M.
507   (2020) Genesis of "silicate exsolution lamellae" in chromite of the Stillwater Complex:
508   A challenge to the high-pressure crystallization of ophiolitic chromitite. Lithos, 378-379,
509   105796.

510   Maruyama, S., Santosh, M. and Zhao, D. (2007) Superplume, supercontinent, and
511   post-perovskite: Mantle dynamics and anti-plate tectonics on the Core-Mantle Boundary.
512   Gondwana Research, 11, 7-37.

513   Marchesi, C., González-Jiménez, J.M., Gervilla, F., Garrido, C.J., Griffin, W.L., O'Reilly,
514   S.Y., Proenza, J.A. and Pearson, N.J. (2011) In situ Re-Os isotopic analysis of
515   platinum-group minerals from the Mayarí–Cristal ophiolitic massif (Mayarí–Baracoa
516   Ophiolitic Belt, eastern Cuba): implications for the origin of Os-isotope heterogeneities
517   in podiform chromitites. Contributions to Mineralogy and Petrology, 161, 977–990

518   Matveev, S. and Ballhaus, C. (2002). Role of water in the origin of podiform chromitite
519   deposits. Earth & Planetary Science Letters, 203(1), 235–243.

520   McGowan N M, Griffin W L, González-Jiménez J M, et al. (2015) Tibetan chromitites:
521   Excavating the slab graveyard. Geology, 43(2), 179–182.

522 Melcher, F., Grum, W. and Simon, G. (1997) Petrogenesis of the ophiolitic giant chromite
523   deposits of Kempirsai, Kazakhstan: A study of solid and fluid inclusions in chromite.
524   Journal of Petrology, 38, 1419–1458.

525 Pagé, P. and Barnes, S.J. (2009) Using trace elements in chromites to constrain the origin of
526   podiform chromitites in the Thetford Mines ophiolite, Quebec, Canada. Economic
527   Geology, 104, 997-1018.

528 Pagé, P., Bédard, J.H., Schroetter, J.-M. and Tremblay, A. (2008) Mantle petrology and
529   mineralogy of the Thetford Mines ophiolite complex. Lithos, 100, 255–292.

530 Prichard, H.M., Neary, C.R., Fisher, F.C. and O'Hara, M.J. (2008) PGE-rich podiform
531   chromitites in the Al'Ays ophiolite complex, Saudi Arabia: an example of critical mantle
532   melting to extract and concentrate PGE. Economic Geology, 103, 1507–1529

533 Pogge von Strandmann, P.A.E., Strandmann, P.A.E., Elliott, E., Marschall, H.R., Coath, C.,
534   Lai, Y.J., Jeffcoate, A.B., and Ionov, D.A. (2011) Variations of Li and Mg isotope ratios
535   in bulk chondrites and mantle xenoliths. Geochimica Et Cosmochimica Acta, 75, 5247–
536   5268.

537 Pearce, J.A., Barker, P.F., Edwards, S.J., Parkinson, I.J. and Leat, P.T. (2000) Geochemistry
538   and tectonic significance of peridotites from the South Sandwich arc-basin system, South
539   Atlantic. Contributions to Mineralogy and Petrology, 139, 36–53.

540 Qiu Tian, Yang Jingsui, Wu Weiwei, et al. (2021) Petrogensis of chromitites and its records
541   of Ti metasomatism in crust-mantle transition zone, Bulqiza ophiolite massif, Albania.
542   Sedimentary Geology and Tethyan Geology, 41, 485–504(in Chinese with English
543   abstract).

544 Satsukawa, T., Griffin, W.L., Piazolo, S. and O'Reilly, S.Y. (2015) Messengers from the
545   deep: Fossil wadsleyite–chromite microstructures from the Mantle Transition Zone.
546   Scientific Reports, 5, 16484.

547 Schauble E. A. (2011) First-principles estimates of equilibrium magnesium isotope
548   fractionation in silicate, oxide, carbonate and hexaaquamagnesium (2+) crystals.
549   Geochimica Et Cosmochimica Acta, 75, 844-869.

550   Seyler, M., Lorand, J.P., Dick, H.J.B. and Drouin, M. (2007) Pervasive melt percolation
551   reactions in ultra-depleted refractory harzburgites at the Mid-Atlantic Ridge, 15º 20´N:
552   ODP Hole 1274A. Contributions to Mineralogy and Petrology, 153, 303–319.

553   Shi, R.D., Alard, O., Zhi, X.C., et al. (2007) Multiple events in the Neo-Tethyan oceanic
554   upper mantle: evidence from Ru–Os–Ir alloys in the Luobusa and Dongqiao ophiolitic
555   podiform chromitites, Tibet. Earth & Planetary Science Letters, 26, 33–48.

556   Spandler, C., O'Neill, H.S. and Kamenetsky, V.S. (2007) Survival times of anomalous melt
557   inclusions from element diffusion in olivine and chromite. Nature, 447, 303–306.

558   Suhr, G., Seck, H.A., Shimizu, N. and Gunther, D. (1998) Infiltration of refractory melts into
559   the lowermost oceanic crust: Evidence from dunite- and gabbro-hosted clinopyroxenes in
560   the Bay of Islands ophiolite. Contributions to Mineralogy Petrology, 131,136–154.

561   Su, B.X., Teng, F.Z., Hu, Y., Shi, R.D., Zhou, M.F., Zhu, B., Liu, F., Gong, X.H., Huang,
562   Q.S., Xiao, Y., Chen, C. and He, Y.S. (2015) Iron and magnesium isotope fractionation
563   in oceanic lithosphere and sub-arc mantle: perspectives from ophiolites. Earth &
564   Planetary Science Letters, 430, 523–532.

565   Su, B.X., Hu, Y., Teng, F.Z., Xiao, Y., Zhang H.F., Sun, Y., Bai, Y., Zhu, B., Zhou, X. H. and
566   Ying, J.F. (2019) Light Mg isotopes in mantle-derived lavas caused by chromite
567   crystallization, instead of carbonatite metasomatism. Earth & Planetary Science Letters,
568   522, 79– 86.

569   Su, B., Robinson, P.T., Chen, C., Xiao, Y., et al. (2020) The occurrence, origin and fate of
570   water in chromitites in ophiolites. American Mineralogist, 105, 894–903.

571   Su, B., Chen, C., Xiao, Y., Robinson, P.T., Liu, X., Wang, J., Uysal, I., Bai, Y. and Sun, Y.
572   (2021a) The Critical Role of Fluid-Mediated Diffusion in Anomalous Fe-Mg-O Isotope
573   Fractionations in Ultramafic Rocks of Ophiolites. Journal of Geophysical Research:
574   Solid Earth, 126(4): e2020JB020632

575   Su, B.X., Liu, X., Robinson, P.T., et al. (2021b) A new model for chromtitie formation in
576   ophiolite: Fluid immiscibility. Science China Earth Sciences, 64, 200

577   Sio, C.K.I., Dauphas, N., Teng, F.Z., Chaussidon, M., Helz, R.T. and Roskosz, M. (2013)
578   Discerning crystal growth from diffusion profiles in zoned olivine by in situ Mg–Fe
579   isotopic analyses. Geochimica Et Cosmochimica Acta, 123, 302–321

580   Teng, F.Z., Wadhwa, M. And Helz, R.T. (2007) Investigation of magnesium isotope
581   fractionation during basalt differentiation: implications for a chondritic composition of
582   the terrestrial mantle. Earth & Planetary Science Letters, 261, 84–92

583   Teng, F.Z., Li, W.Y., Ke, S., Marty, B., Dauphas, N., Huang, S., Wu, F.Y. and Pourmand, A.
584   (2010a) Magnesium isotopic composition of the Earth and chondrites. Geochimica Et
585   Cosmochimica Acta, 74, 4150–4166.

586   Teng, F.Z., Li, W.Y., Rudnick, R.L. and Gardner, L.R. (2010b) Contrasting lithium and
587   magnesium isotope fractionation during continental weathering. Earth & Planetary
588   Science Letters, 300, 63–71.

589   Teng, F.Z., Dauphas, N., Helz, R.T., Gao, S. and Huang, S. (2011) Diffusion-driven
590   magnesium and iron isotope fractionation in Hawaiian olivine. Earth & Planetary Science
591   Letters, 308, 317–324.

592   Wirth, R. (2009) Focused Ion Beam FIB: combined with SEM and TEM: Advanced analytical
593   tools for studies of chemical composition, microstructure and crystal structure in
594   geomaterials on a nanometre scale. Chemical Geology, 261, 217–229.

595   Wang, J., Su, B.X., Robinson, P.T., Bai, Y., Liu, X., Sakyi, P.A., Jing, J.J., Chen, C., Liang,
596   Z. And Bao, Z.A. (2021) Trace elements in olivine: Proxies for petrogenesis,
597   mineralization and discrimination of mafic – ultramafic rock. Lithos, 388-389: 106085.

598   Xiao, Y., Teng, F.Z., Su, B.X., Hu, Y., Zhou, M.F., Zhu, B., Shi, R.D., Huang, Q.S., Gong,
599   X.H. and He, Y.S. (2016) Iron and magnesium isotopic constraints on the origin of
600   chemical heterogeneity in podiform chromitite from the Luobusa ophi- olite, Tibet.
601   Geochemistry, Geophysics, Geosystems, 17, 940–953.

602   Xiong, F.H., Yang, J.S., Liu, Z., Guo, G.L., Chen, S.Y., Xu, X.Z., Li, Y. And Liu, F. (2013)
603   High-Cr and high-Al chromitite found in western Yarlung-Zangbo suture zone in Tibet.
604   Acta Petrologica Sinica, 29, 1878–1908. (in Chinese with English abstract).

605   Xiong, F.H., Yang, J.S., Robinson, P.T., Xu, X.Z., Liu, Z., Li, Y., Li, J.Y. and Chen, S.Y.

606   (2015) Origin of podiform chromitite, a new model based on the Luobusa ophiolite,

607   Tibet. Gondwana Research, 27, 525–542.

608   Xiong, F.H., Yang, J.S., Xu, X.Z., Kapsiotis, A., Hao, X.L. and Liu, Z. (2018) Compositional

609   and isotopic heterogeneities in the Neo-Tethyan upper mantle recorded by coexisting

610   Al-rich and Cr-rich chromitites in the Purang peridotite massif, SW Tibet (China).

611   Journal of Asian Earth Sciences, 159, 109–129

612   Xiong, F.H., Liu, Z., Kapsiotis, A., Yang, J.S., Lenaz, D. and Robinson, P.T. (2019)

613   Petrogenesis of lherzolites from the Purang ophiolite, Yarlung-Zangbo Suture Zone,

614   Tibet: origin and significance of ultra-high pressure and other "unusual" minerals in the

615   Neo-Tethyan lithospheric mantle. International Geology Review, 17, 2184-2210.

616   Xiong, F.H., Xu, X.Z., Mugnaioli, E., Gemmi, M., Wirth, R., Grew, E.S., Robinson, P.T. and

617   Yang, J.S. (2020a) Two new minerals, badengzhuite, TiP, and zhiqinite, $TiSi_2$, from the

618   Cr-11 chromitite orebody, Luobusa ophiolite, Tibet, China: is this evidence for

619   super-reduced mantle-derived fluid? European Journal of Mineralogy, 32, 557-574

620   Xiong, F.H., Meng, Y.K., Yang, J.S., Liu, Z., Xu, X.Z., Eslami, A. and Zhang, R. (2020b)

621   Geochronology and petrogenesis of the mafic dykes from the Purang ophiolite:

622   Implications for evolution of the western Yarlung-Tsangpo suture zone, southwestern

623   Tibet. Geoscience Frontiers, 11, 277–292.

624   Xiong, F.H., Dilek, Y., Xu, X.Z. and Yang, J.S. (2020c) Opx–Cpx exsolution textures in

625   lherzolites of the Cretaceous Purang Ophiolite (S. Tibet, China), and the deep mantle

626   origin of Neotethyan abyssal peridotites. International Geology Review, 62, 665-682.

627   Xu, X.Z., Cartigny, P., Yang, J.S., Dilek, Y., Xiong, F.H. and Guo, G.L. (2018) Fourier

628   transform infrared spectroscopy data and carbon isotope characteristics of the

629   ophiolite-hosted diamonds from the Luobusa ophiolite, Tibet, and Ray-Iz ophiolite, Polar

630   Urals. Lithosphere, 10(1), 156–169.

631   Yamamoto, S., Komiya, T., Hirose, K. and Maruyama, S. (2009) Coesite and clinopyroxene

632   exsolution lamellae in chromites: In-situ ultrahigh-pressure evidence from podiform

633   chromitites in the Luobusa ophiolite, southern Tibet. Lithos, 109, 314–322.

27

Yang, J., Meng, F., Xu, X., et al. (2015) Diamonds, native elements and metal alloys from chromitites of the Ray-Iz ophiolite of the Polar Urals. Gondwana Research, 27(2), 459–485

Yang, J.S., Dobrzhinetskaya, L., Bai, W.J., Fang, Q.S., Robinson, P.T., Zhang, J. and Green, H.W. (2007) Diamond-and coesite-bearing chromitites from the Luobusa ophiolite, Tibet. Geology, 35, 875–878.

Yang, J.S., Robinson, P.T. and Dilek, Y. (2014) Diamonds in Ophiolites: a little – known diamond occurrence. Elements, 10, 123–126.

Yang, J.S., Xu, X.Z., Li, Y., Li, J.Y., Rong, H., Ba, D.Z. and Zhang, Z.M. (2011) Diamonds recovered from peridotite of the Purang ophiolite in the Yarlung–Zangbo suture of Tibet: A proposal for a new type of diamond occurrence. Acta Petrologica Sinica, 27, 3207–3222. (in Chinese with English abstract).

Yang, W., Teng, F.Z. and Zhang, H.F. (2009) Chondritic magnesium isotopic composition of the terrestrial mantle: a case study of peridotite xenoliths from the North China craton. Earth & Planetary Science Letters, 288, 475–482.

Young, E.D., Tonui, E., Manning, C.E., Schauble, E.A. and Macris, C. (2009) Spinel-olivine magnesium isotope thermometry in the mantle and implications for the Mg isotopic composition of Earth. Earth & Planetary Science Letters, 288, 524–533.

Young, E.D., Manning, C.E., Schauble, E.A., Shahar, A., Macris, C.A., Lazar, C. and Jordan, M. (2015) High-temperature equilibrium isotope fractionation of non-traditional stable isotopes: Experiments, theory, and applications. Chemical Geology, 395, 176–195.

Zaeimnia, F., Arai, S. and Mirmohammadi, M. (2017) Na-rich character of metasomatic/metamorphic fluids inferred from preiswerkite in chromitite pods of the Khoy ophiolite in Iran: Role of chromitites as capsules of trapped fluids. Lithos, 268-271, 351–363.

Zhou, M.F., Robinson, P.T., Su, B.X., Gao, J.F., Li, J.W., Yang, J.S. and Malpas, J. (2014) Compositions of chromite, associated minerals, and parental magmas of podiform chromite deposits: The role of slab contamination of asthenospheric melts in suprasubduction zone envrionments. Gondwana Research, 26, 262-283.

Zhou, M.F. and Robinson, P. (1997) Origin and tectonic environment of podiform chromite deposits. Economic Geology, 92, 259–262

665 **Figure captions:**

666 **Figure 1. (a)** Simplified tectonic map of the Tibetan Plateau, with several terranes separated

667   by well-defined sutures. The (Indus-)Yarlung-Zangbo Suture Zone [(I)YZSZ], the

668   southernmost one of these sutures, separates the Lhasa block to the north from the

669   Tibetan-Himalayan orogenic belt to the south. BNS = Bangong-Nujiang Suture; IYZS =

670   Indus-Yarlung-Zangbo Suture. **(b)** Geological map of the Purang ophiolite massif

671   (modified from Yang et al. 2011; Xiong et al. 2018, 2020b, c). Gab = gabbro, H-dun =

672   Cr_2O_3-rich dunite, L-Dun = Cr_2O_3-poor dunite, Harz = harzburgite, Lhz = lherzolite.

673 **Figure 2.** Field photographs showing the occurrence of chromitite in the Purang massif. **(a)**

674   High-Cr massive chromitite. **(b)** Dunite vein with high-Al massive chromitite laminae.

675   **(c)** Serpentinite with high-Cr massive chromitite. **(d)** High-Al nodular chromitite in a

676   dunitic host rock.

677 **Figure 3. (a)** Compositional variations of chromite grains from the Purang peridotites

678   revealed by the Cr# vs. TiO_2 (wt.%) plot (after Pearce et al. 2000). **(b)** Cr# vs. Mg#

679   diagram with data for chromite grains from peridotite samples of the Purang ophiolite.

680   Fields for abyssal and forearc peridotites are from Dick and Bullen (1984), Ishii et al.

681   (1992), Arai (1997), and Hébert et al. (2003). The degree of melt extraction is calculated

682   from the spinel composition using the empirical formula of Hellebrand et al. (2001).

683   Data of spinel grains from the Purang lherzolites are from Xiong et al. (2019).

29

684   **Figure 4. (a-d)** BSE images of acicular silicate micro-inclusions in chromite grains from the

685   Purang chromitites. **(d)** Plane-polarized light photomicrographs of acicular (Cpx)

686   inclusions in chromite grains from the high-Al chromitites.

687   **Figure 5.** Backscattered (BSE) images of various pyroxene inclusions in chromite grains from

688   the Purang ophiolite**. (a-c)** Octahedral orthopyroxene inclusions. **(d-f)** Subhedral and

689   euhedral clinopyroxene inclusions. **(g-i)** Composite euhedal clinopyroxene and

690   orthopyroxene inclusions in chromite. Cpx = clinopyroxene; Opx = orthopyroxene; Chr

691   = chromite.

692   **Figure 6. (a)** TEM image of a FIB foil showing a single clinopyroxene inclusion in a

693   chromite grain. **(b)** A high-resolution TEM image showing sharp contacts of an acicular

694   inclusion in a high-Al chromite grain. **(c)** EDX spectrum of a Cr-spinel grain. **(d)** EDX

695   spectrum of the lamellar clinopyroxene inclusion. **(e)** EDX spectrum of a high-Cr

696   chromite grain. Note the Ga peaks in the spectrum are due to Ga-ion implantation during

697   the FIB milling and the Cu peaks are due to secondary fluorescence from the copper grid

698   that supports the foil. Cpx = clinopyroxene, Chr = chromite.

699   **Figure 7.** BSE images of mineral inclusions in chromite grains from the Purang chromitites.

700   **(a)** an acicular inclusion about 50 μm long and <1 μm, which is interpreted as an

701   Fe-Si-O-bearing fluid inclusion (see Fig. 9). **(b)** Apatite inclusion along cracks between

702   chromite grains. **(c)** A uvarovite inclusion in chromite. **(d)** A composite

703   serpentine-amphibole-phlogopite-millerite inclusion. **(e)** A composite amphibole-apatite

704   inclusion. **(f)** A composite amphibole-apatite-pentlandite inclusion in chromite. **(g)** An

705   orthopyroxene-amphibole composite inclusion. **(h)** A clinopyroxene-amphibole

706   inclusion in the chromitite. **(i)** A uvarovite inclusion in chromite. Cpx = clinopyroxene;

707   Ap = apatite; Amp = amphibole; Pn = pentlandite; Pg = phlogopite; Mil = millerite; Uva

708   = uvarovite; Chr = chromite.

709   **Figure 8**. BSE images of metal alloys and sulfide inclusions in the Purang chromitites. Mil=

710   millerite; Amp = amphibole; Cc = chalcocite; Gn = galena; Chr= chromite.

711   **Figure 9 (a)** FIB foil of the acicular inclusion shown in Fig. 7a with a vertical feature near the

712   center of the foil. **(b)** TEM image of an acicular clinopyroxene inclusion surrounded by

713   open spaces in a chromite grain. **(c)** EDX spectrum of the same inclusion showing peaks

714   of Fe, Si and O as well as Mg, Al and Cr. The black domains may have been filled with

715   fluids, **(d)** & **(e)** X-ray elemental maps along the orange line across the inclusion,

716   showing major Fe, Si and O peaks. The Cr, Al, and Mg are concentrated in the host

717   chrome spinel.

718   **Figure 10. (a)** TEM image of a uvarovite inclusion in the chromite grain shown in Figure

719   10b. **(b)** EDX spectrum of the uvarovite inclusion showing peaks for Si, O, and Ca and

720   minor peaks for Cr and Fe. The indexed diffraction pattern (Fast Fourier Transform,

721   FFT) showing the upper part of the TEM confirming the isometric structure. **(c)** EDX

722   spectrum of the chromite grain with major Al and Cr peaks. The FFT pattern also shows

723   the isometric structure of the same chromite grain.

724   **Figure 11.** Binary plots of Cr# vs trace element contents (ppm) in chromite grains from the

725   Purang high-Cr and high-Al chromitites.

726   **Figure 12.** MORB-normalized trace element patterns of the Purang chromitites compared to

727   patterns of boninite (BON) and Thetford Mines ophiolite (TMO) chromitites. Reference

728   values are from Barnes et al. (1985) and Pagé et al. (2008).

729   **Figure 13.** Histograms of the Mg isotope composition of peridotites from the Purang

730   ophiolites and from other occurrences. **(a)** δ^{26}Mg signatures of MORB and OIB lavas.

731   The dashed line represents the average δ^{26}Mg values of chondrites (−0.28‰, Teng et al.

732   2010a). **(b)** δ^{26}Mg values of ophiolitic chromitite, mafic and ultramafic rocks and

733   peridotite xenoliths. **(c)** δ^{26}Mg compositions of the different lithological units of the

734   Purang ophiolite.

735   Magnesium isotope data sources: MORBs, Bourdon et al. (2010), Teng et al. (2010b);

736   OIBs, Teng et al. (2007, 2010a), Bourdon et al. (2010); peridotite xenoliths, Yang et al.

737   (2009), Young et al. (2009), Bourdon et al. (2010), Teng et al. (2010b), Huang et al.

738   (2011), Pogge von Strandmann et al. (2011); mafic and ultramafic ophiolites, Su et al.

739   (2015).

740

741   **Table captions:**

742   **Table 1.** Representative EPMA data of chromite grains from the Purang chromitites (wt.%).

743   **Table 2.** Representative EPMA data of silicate inclusions in chromite grains from the Purang

744   chromitites (wt.%).

745   **Table 3.** Trace element composition, by LA-ICP-MS, of chromite grains from the Purang

746   chromitites (ppm).

747   **Table 4.** Mg isotopic compositions of selected samples from the Purang chromitites and

748   associated peridotites.

749

750   **Supplementary Material 1.** Lithological subdivision of chromitite-dunite associations in the

751   Purang ophiolite (South Tibet)

752   **Supplementary Material 2.** (a-h) X-ray elemental maps of the acicular inclusions in

753   chromite grains from the Purang chromitites.

754   **Supplementary Material 3.** Raman spectra for an acicular inclusion (same as in Fig. 4), with

755   clinopyroxene and chromite peaks.

756   **Supplementary Material 4.** Back-scattered-electron (BSE) images of amphibole, phlogopite

757   inclusions from Purang chromitite.

758   **Supplementary Material 5.** X-ray elemental maps of a Ru-Os-Ir-Fe-Ni inclusion in the a

759   chromite grain from the Purang chromitite.

760   **Supplementary Material 6.** BSE images and X-ray elemental maps of a wüstite inclusion in

761   chromite with a major FeO component.

762   **Supplementary Material 7.** Mg isotopic signatures of olivine, orthopyroxene, and chromite

763   concentrates as well as whole-rock data for the associated lithologies (Xiao et al. 2016

764   and references therein).

765

(a)

EURASIA

North China Craton

Altyn Tagh Fault

Tarim Basin

Qaidam Bsin

Qilian Orogenic Belt

Kunlun range

Songpan-Gangzi Terrane

Hoh-Xil Basin

Qiangtang Terrane

Karakorum Fault

Western Syntaxis

Ritu

Dongbo

Gaize

Dongco

Fig.b

Purang

Dangqiong

BNS

Dongqiao

Amdo

Dingqing

Lhasa Terrane

YZS

Saga

Xigaze

Luobusa

Eastern Syntaxis

South China Craton (Yangtze Block)

Tibetan - Himalayan Orogenic belt

INDIA

N

Ophiolite

0   100   200 km

(b)

E80°45′   E81°00′   E81°15′

N30°50′

P2-3
J2
N2-Q
Harz
P2-3
J2
Jiangyema
H-Dun
H-Dun
H-Dun
L-Dun
Harz
N2-Q
Purang
H-Dun
H-Dun
Harz
Harz
Harz
K2
C1
D1-2
Maiduoding
C1
D1-2
C1
K1

P2-3
E2
H-Dun
Lhz
Harz
H-Dun
K2
Lhz
K2
K2
H-Dun
Lhz
Massif
Harz

C1-2
D3
Shasezuo
D3
C1-2
K2
J1
C1-2
J1
Aba
T1-2
K2

N2-Q
D1-2
D3
C1-2
T1-2
K2
N2-Q

Harz
Laangcuo
H-Dun
Harz
H-Dun
Gab
Gran
Gran

0 2 4km

N30°50′

N30°40′

N30°30′

E80°45′   E81°00′   E81°15′

PURANG MASSIF (140-120 Ma)

- Gab — Gabbro
- H-Dun — Cr₂O₃-rich Dunite
- L-Dun — Cr₂O₃-poor Dunite
- Harz — Harzburgite
- Lhz — Lherzolite
- K2 — Ophiolitic mélange (Cretaceous)

TETHYAN HIMALAYA OF SOUTHERN TIBET (Paleozoic-Cretaceous)

- N2-Q — Neogene-Quaternary
- Gran — Leucogranite (28-8 Ma)
- K1 — Cretaceous mélange
- J2 — Upper Jurassic siltstone
- J1 — Early Jurassic mélange
- T1 — Lower Triassic
- P2-3 — UpperPermian
- C1-2 — Lower Carboniferous
- D3 — Upper Devonian
- D1-2 — Lower Devonian

SYMBOLS

- ★ High-Cr chromitite
- ★ High-Al chromitite
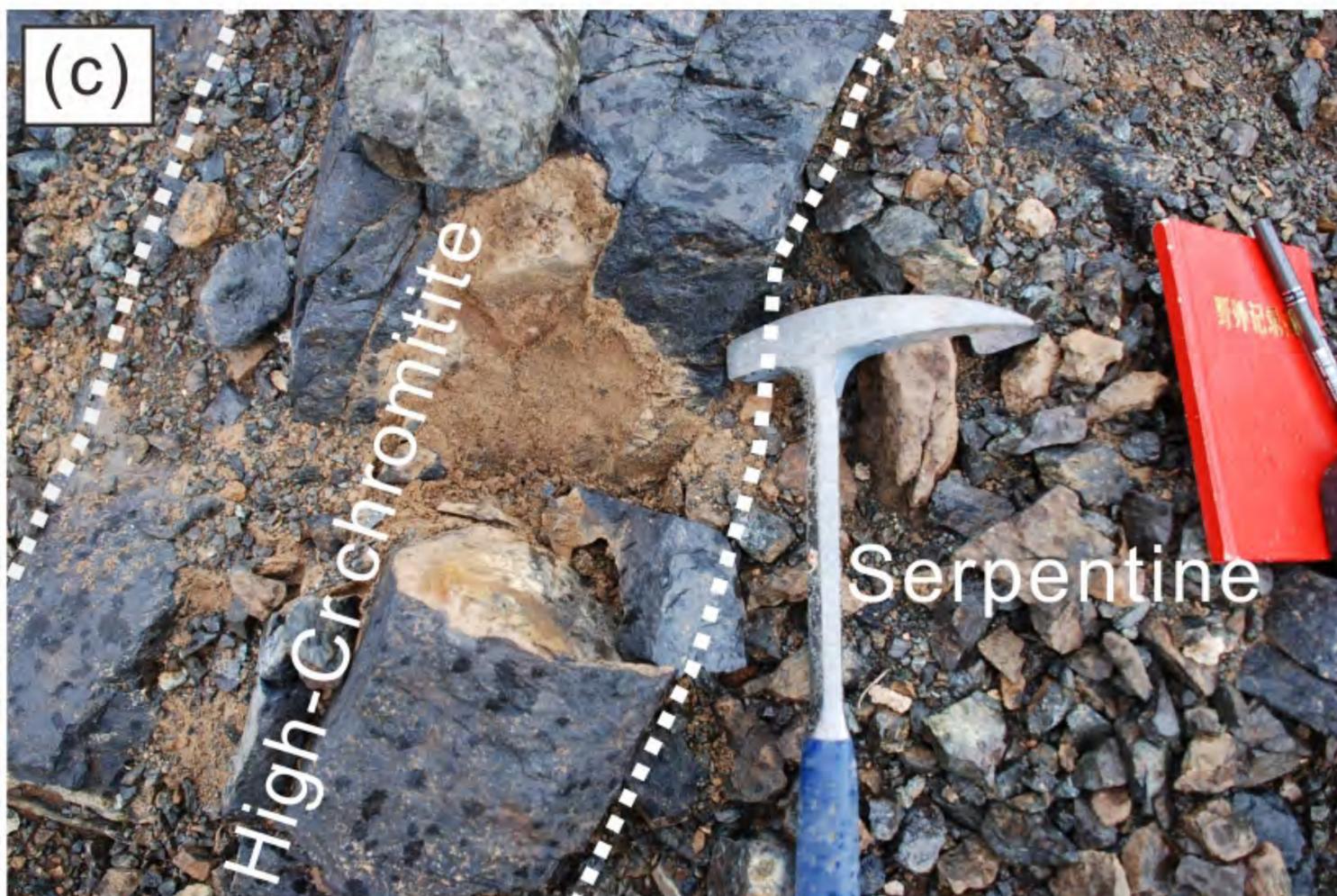- Thrust fault contact
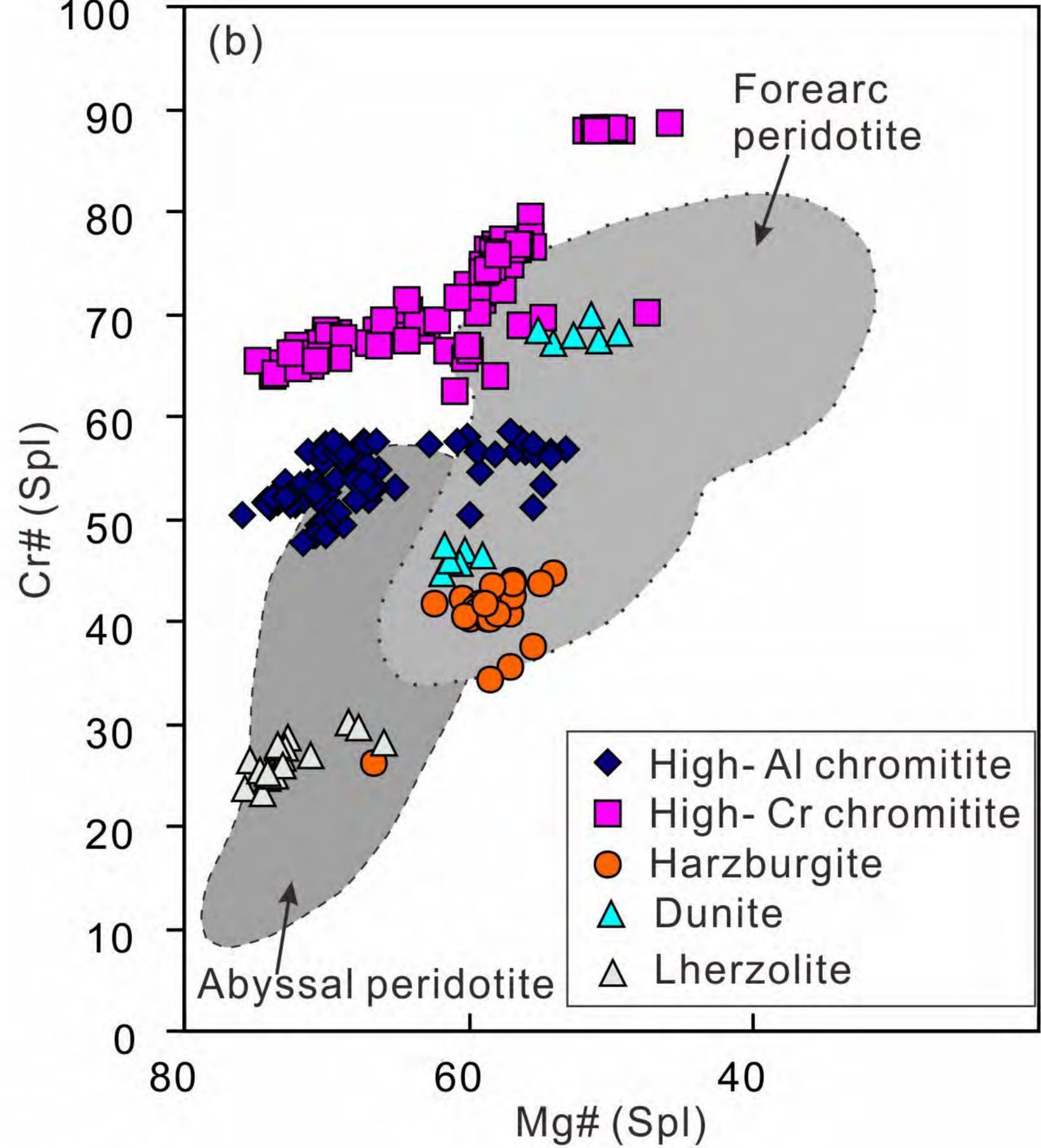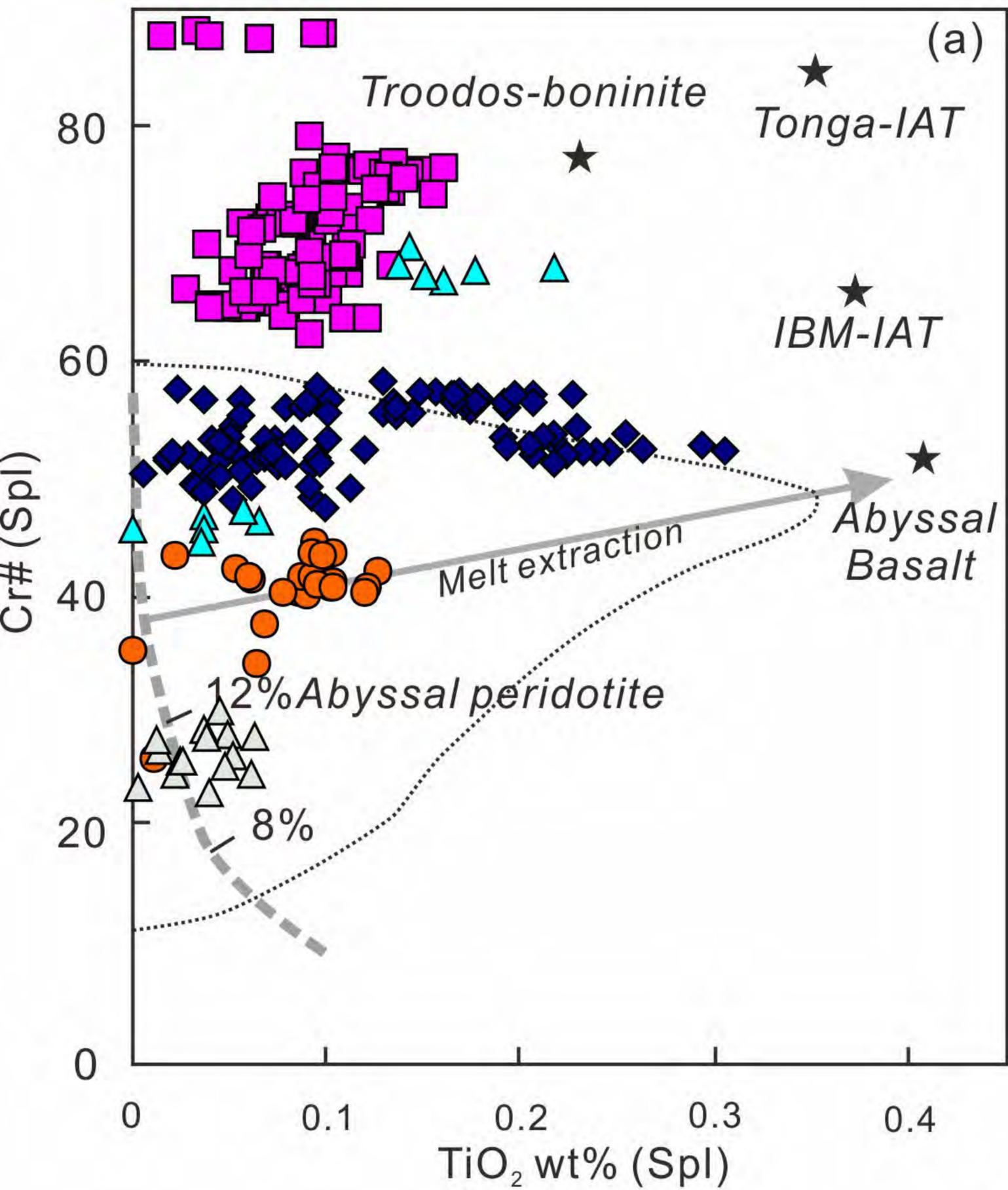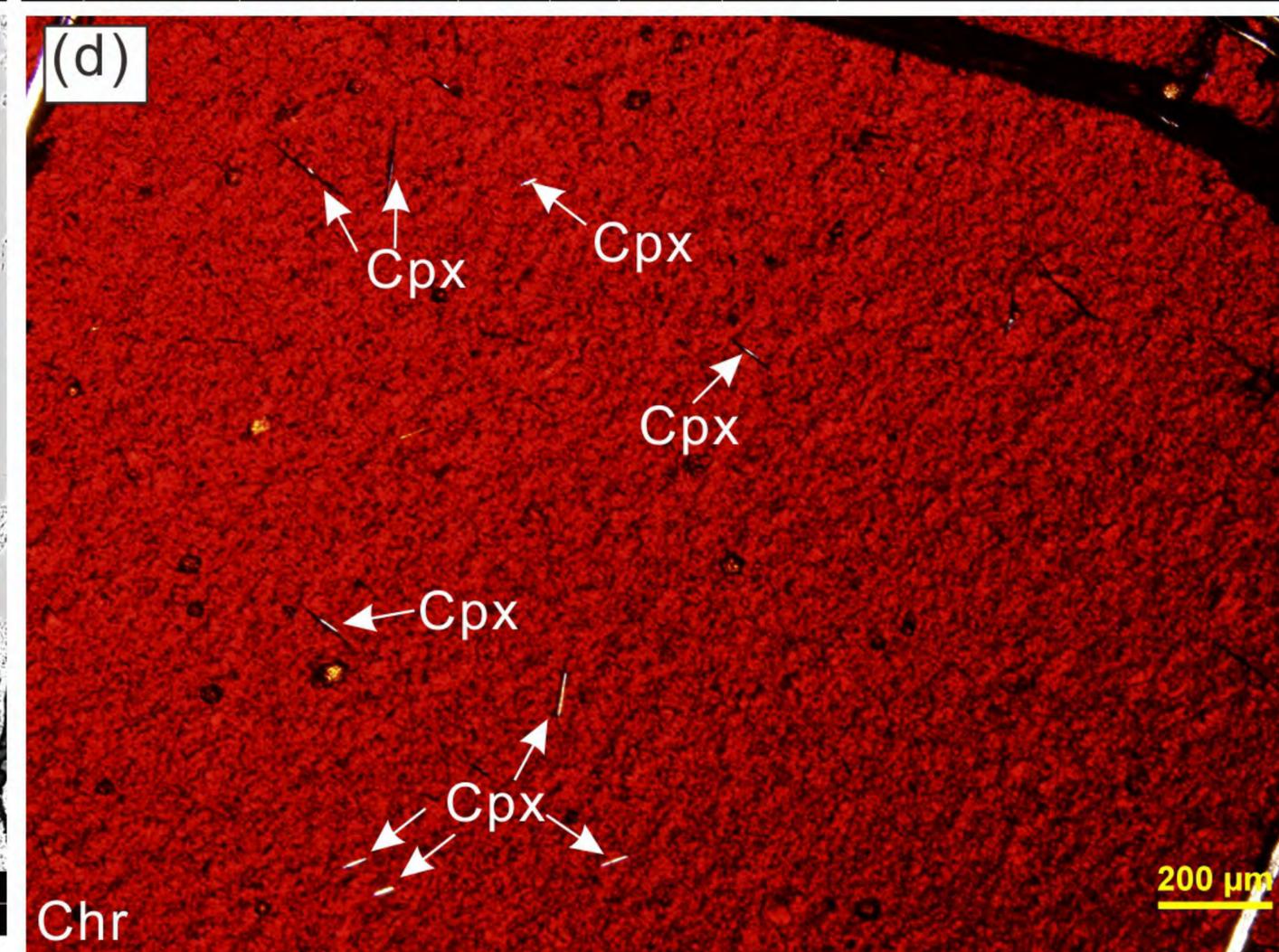- Undifferentiated fault
- River

Figure 1

Figure 2

Figure 3
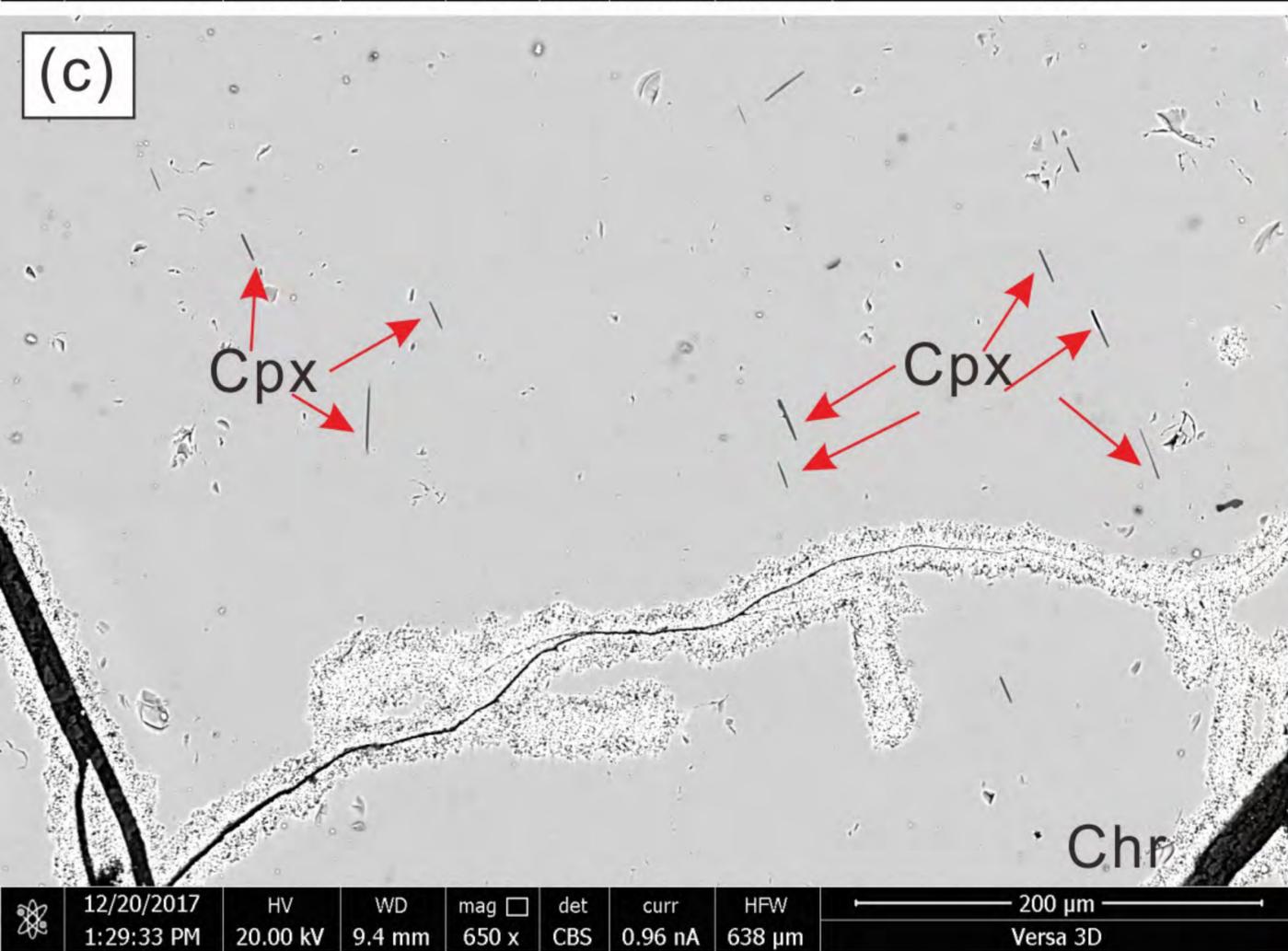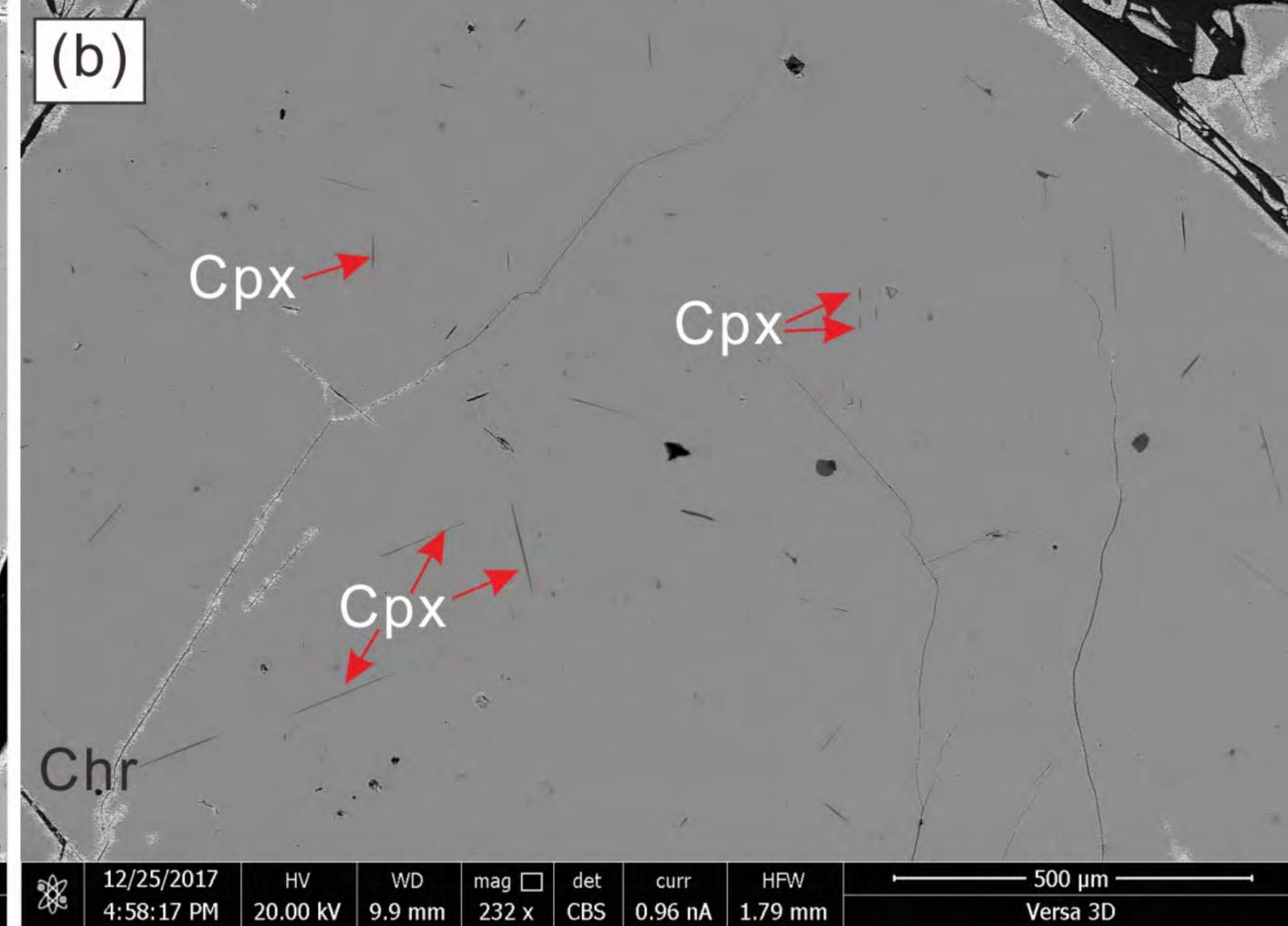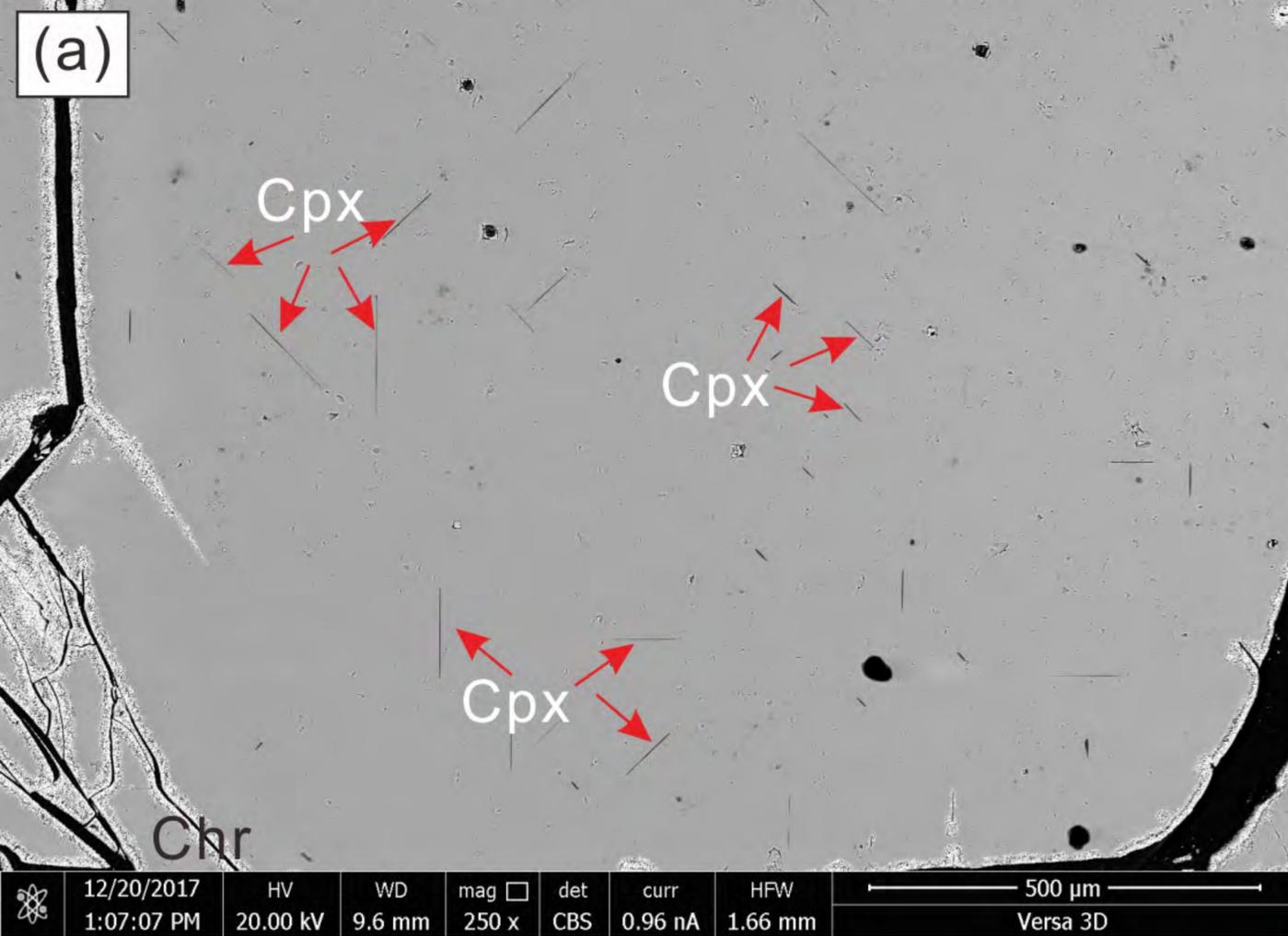
Figure 4
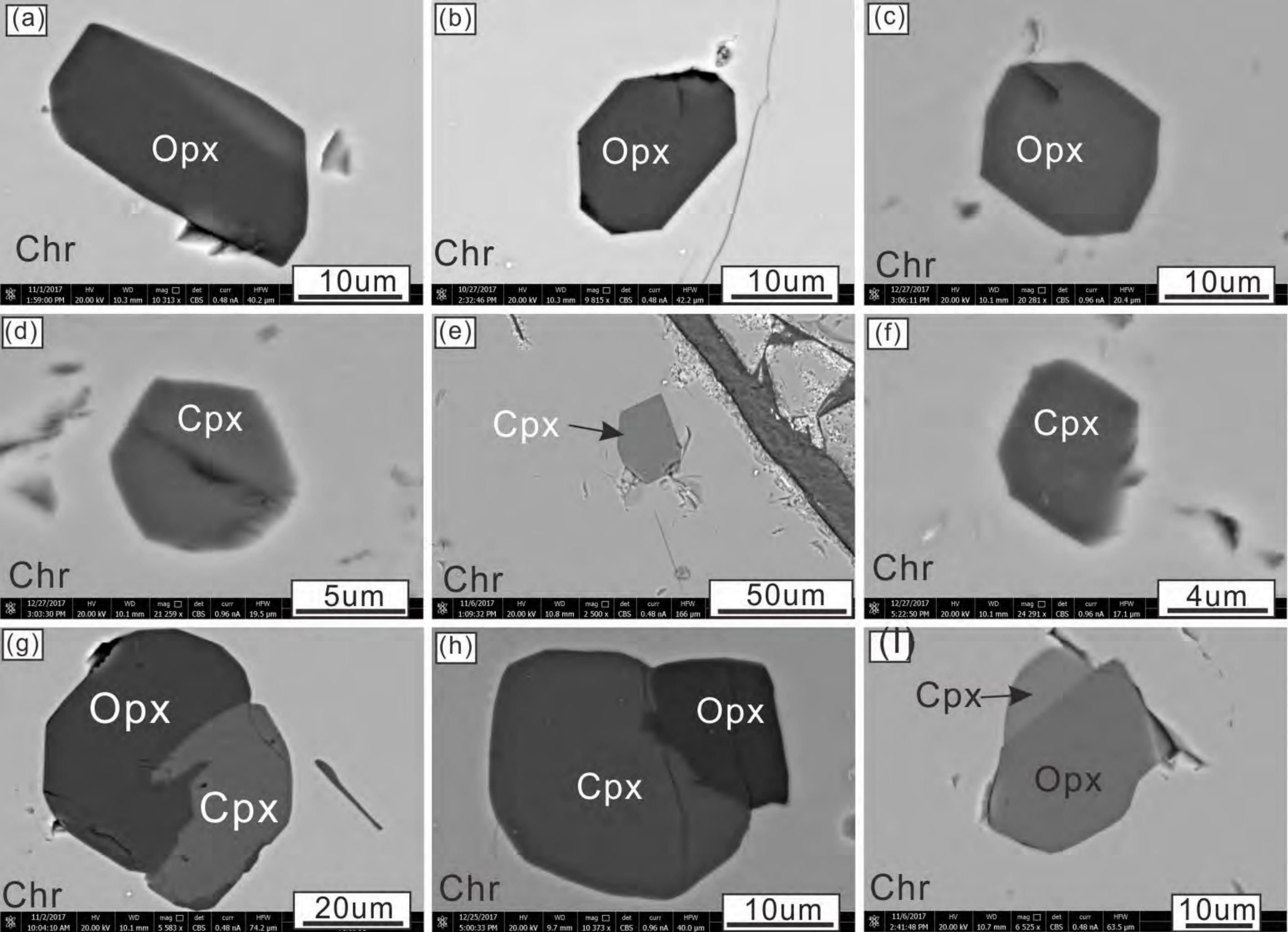
Figure 5
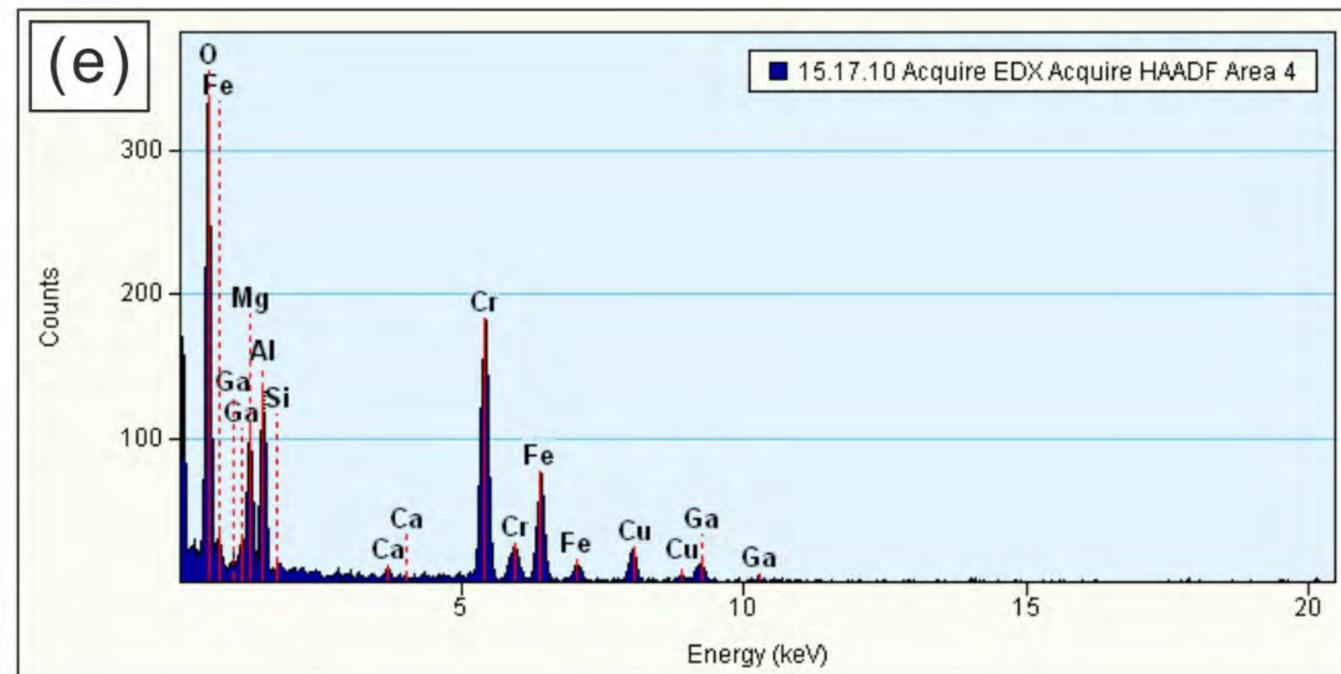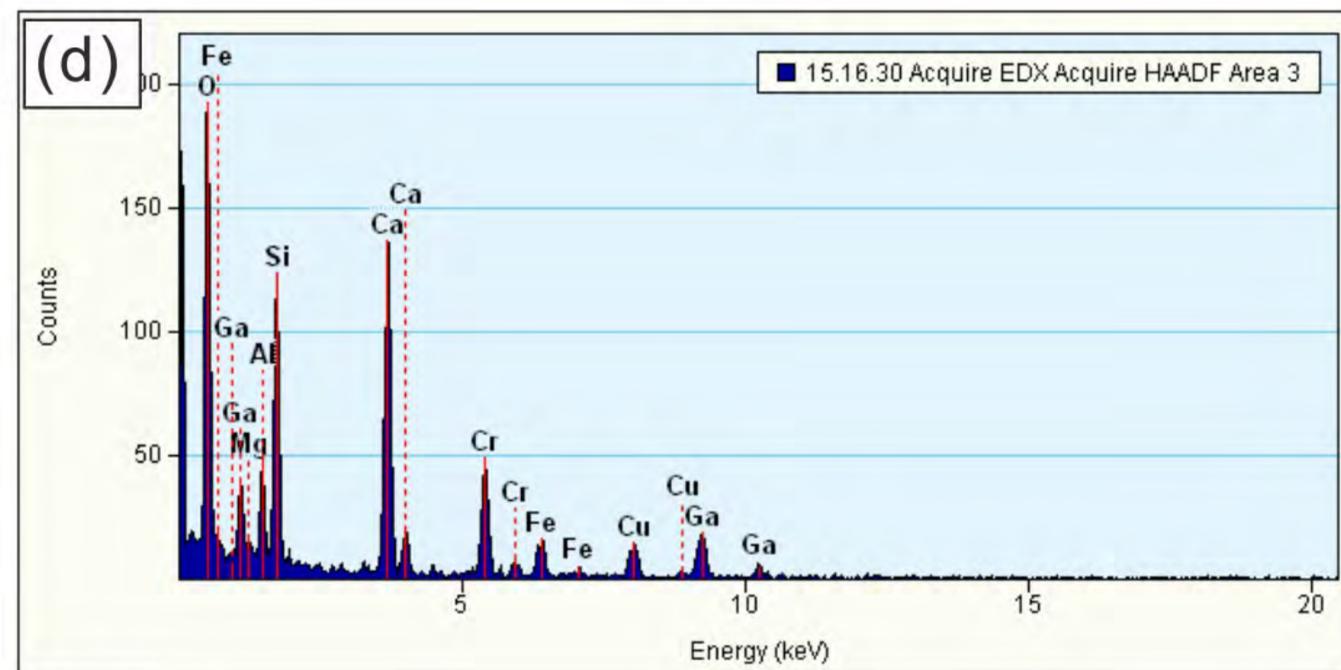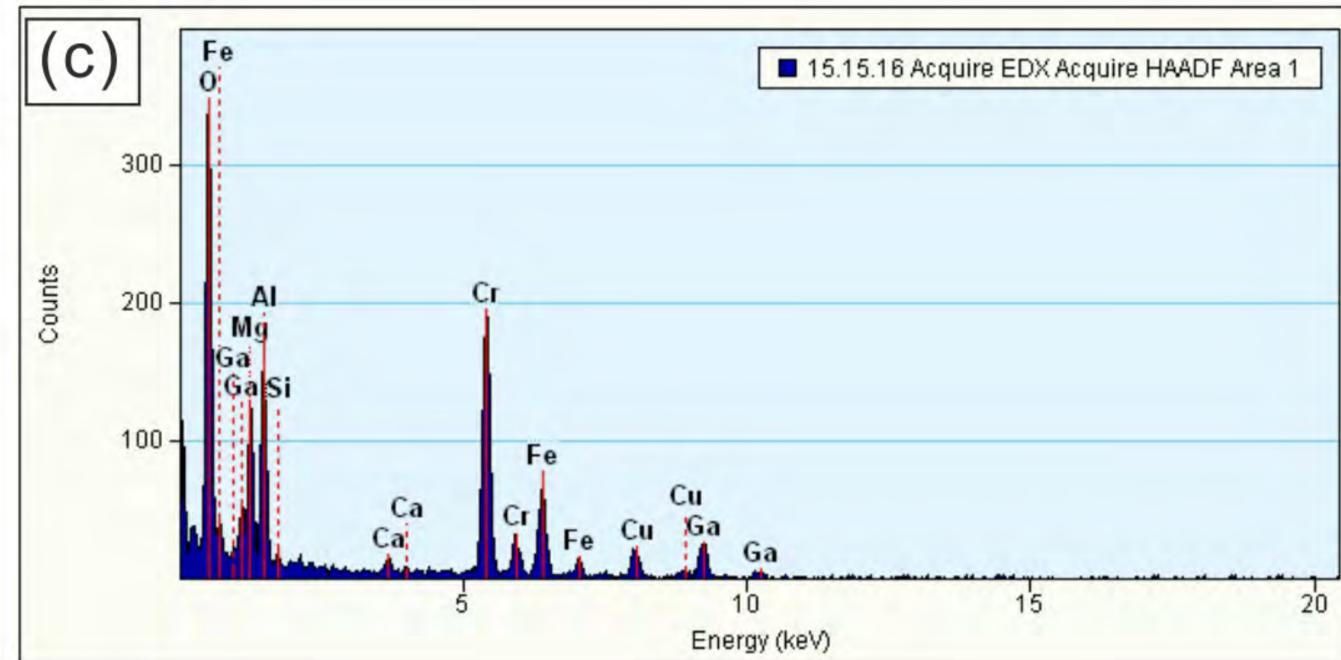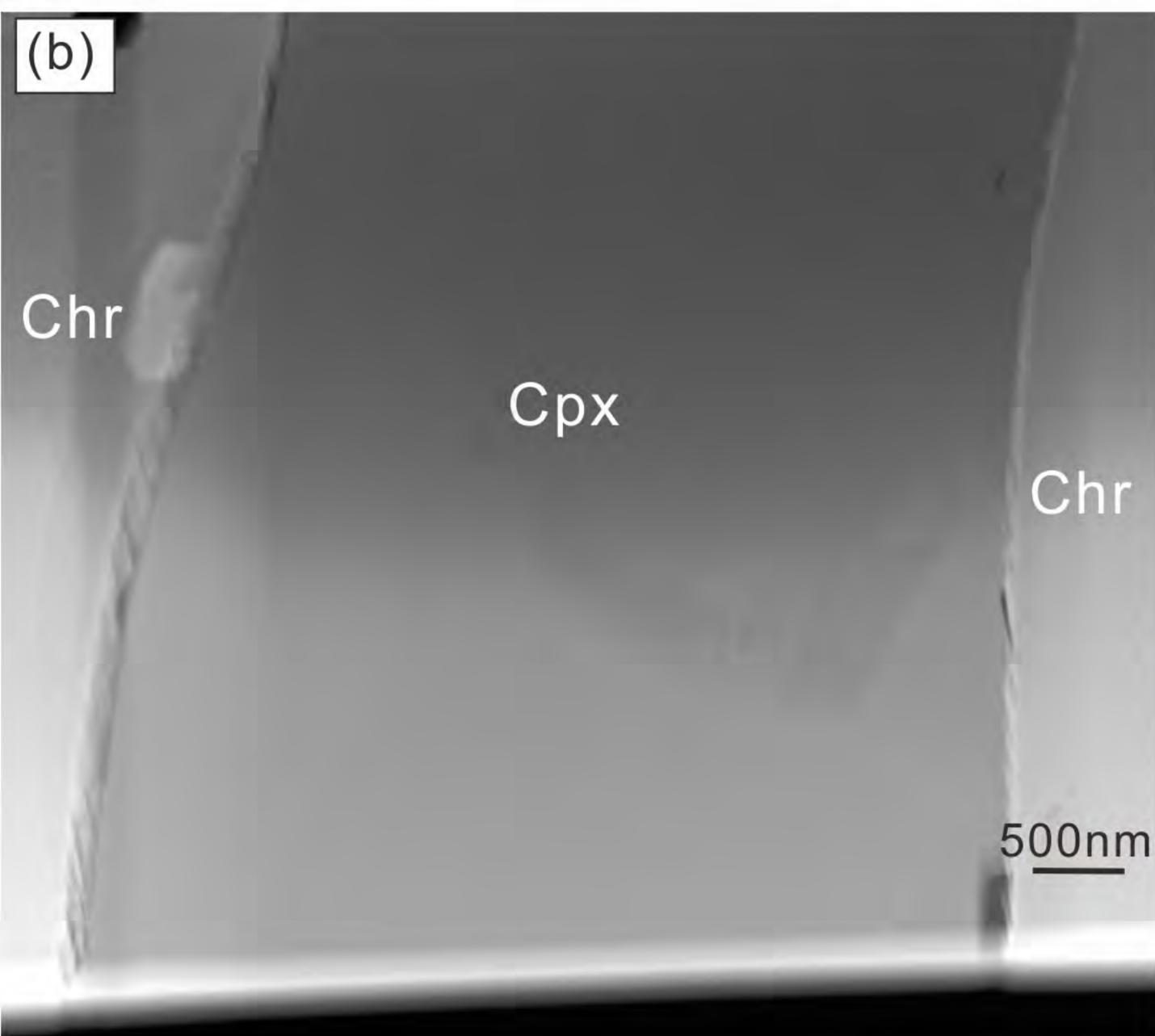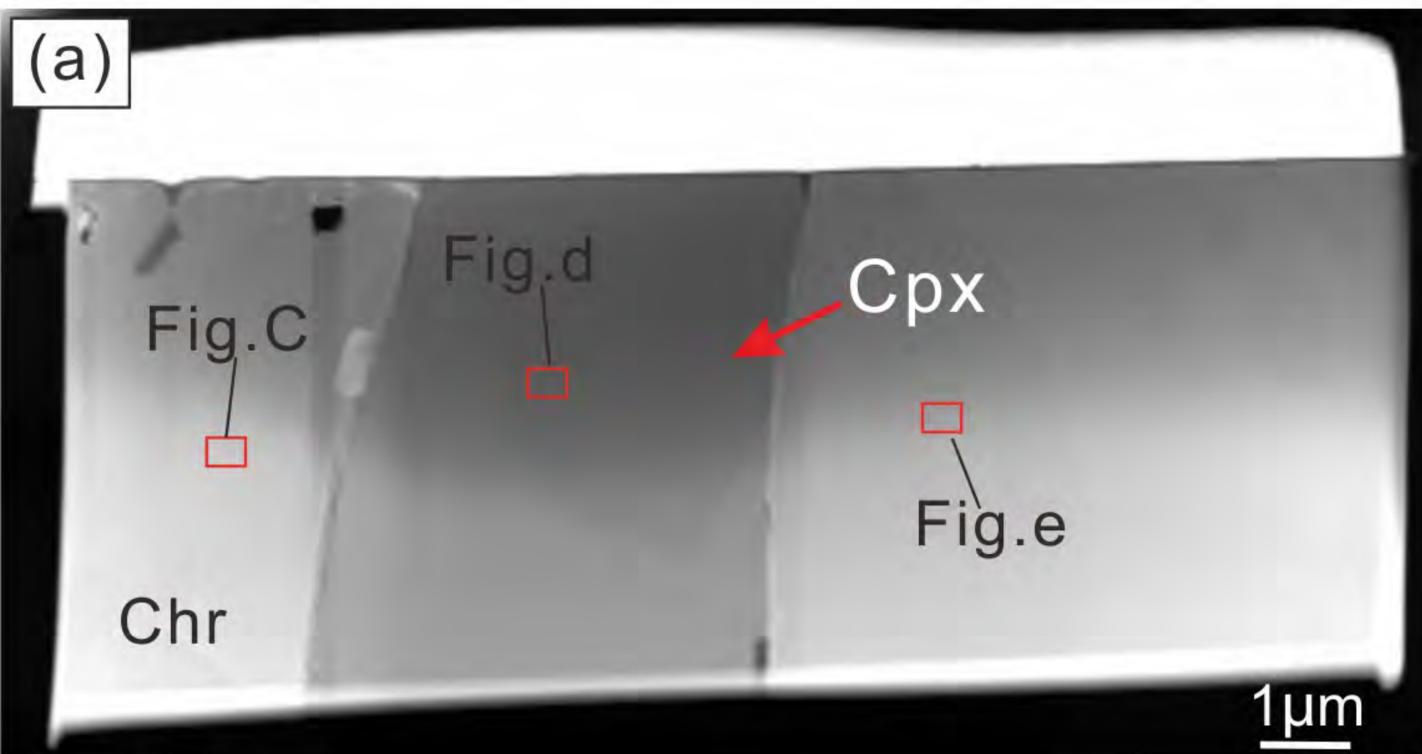
Figure 6
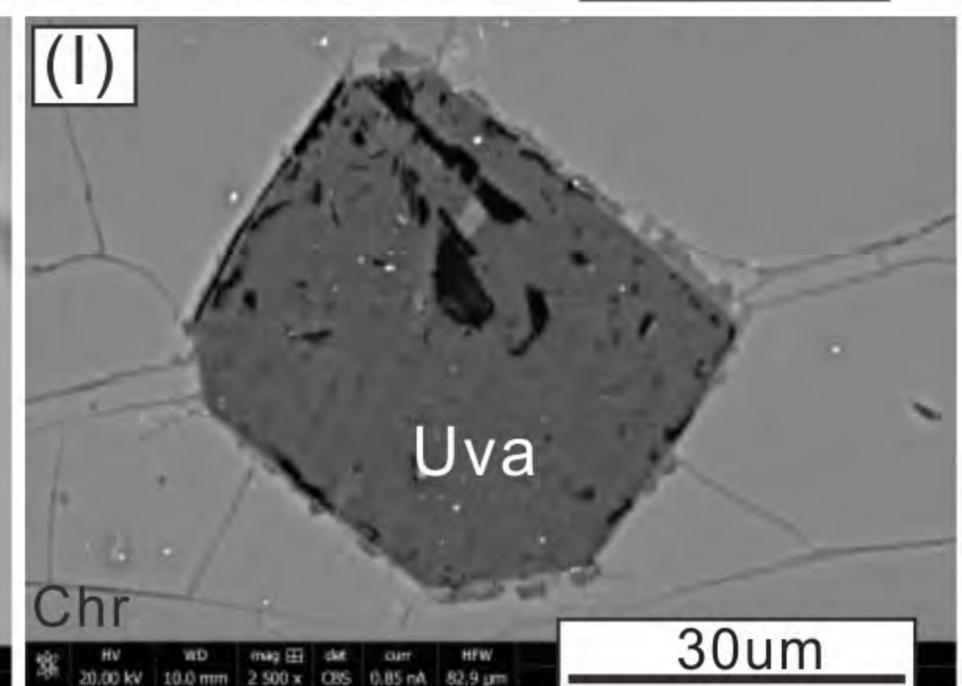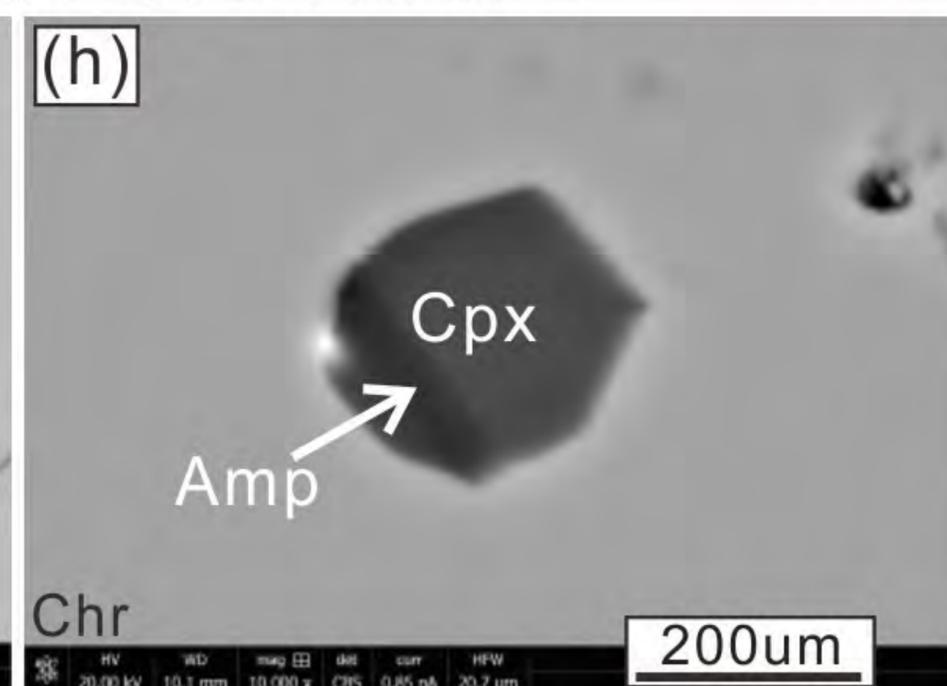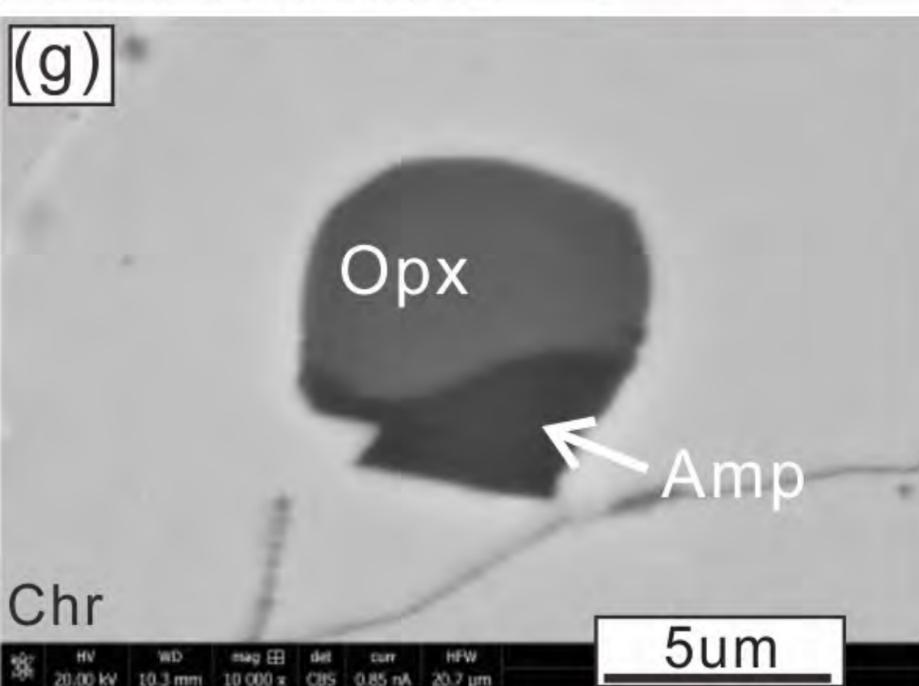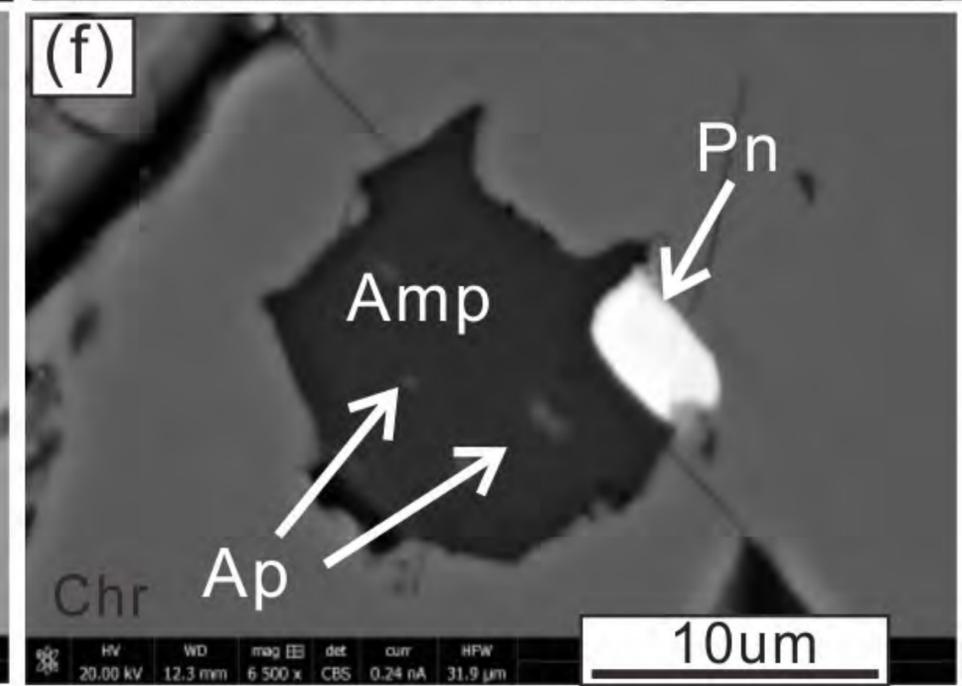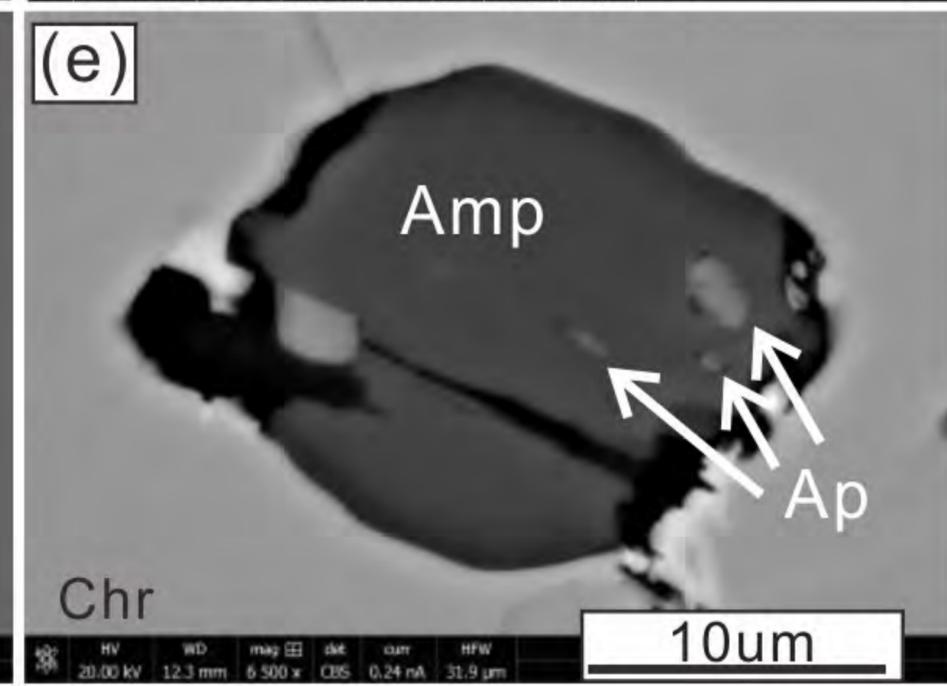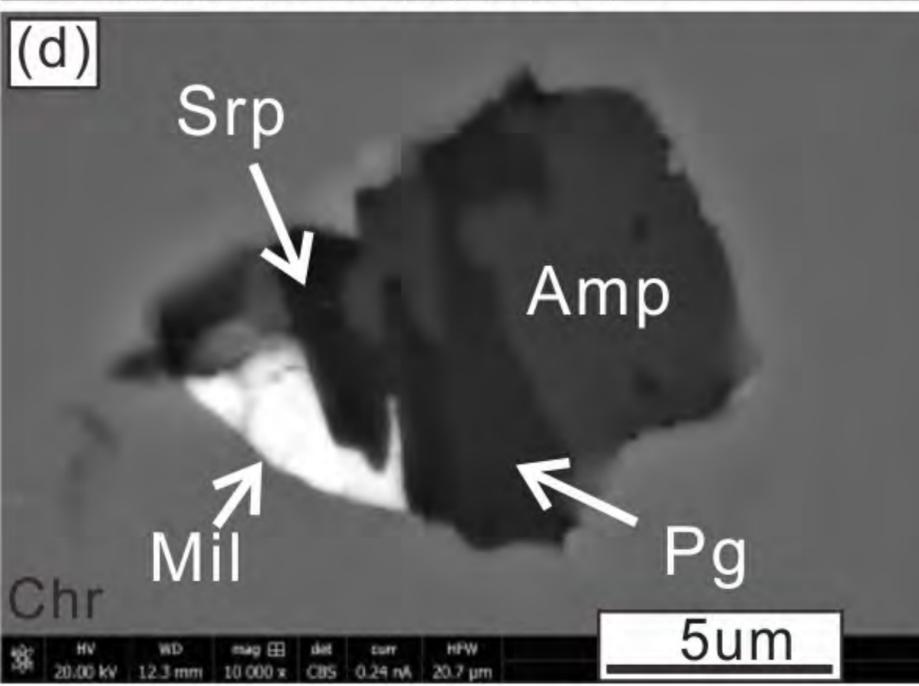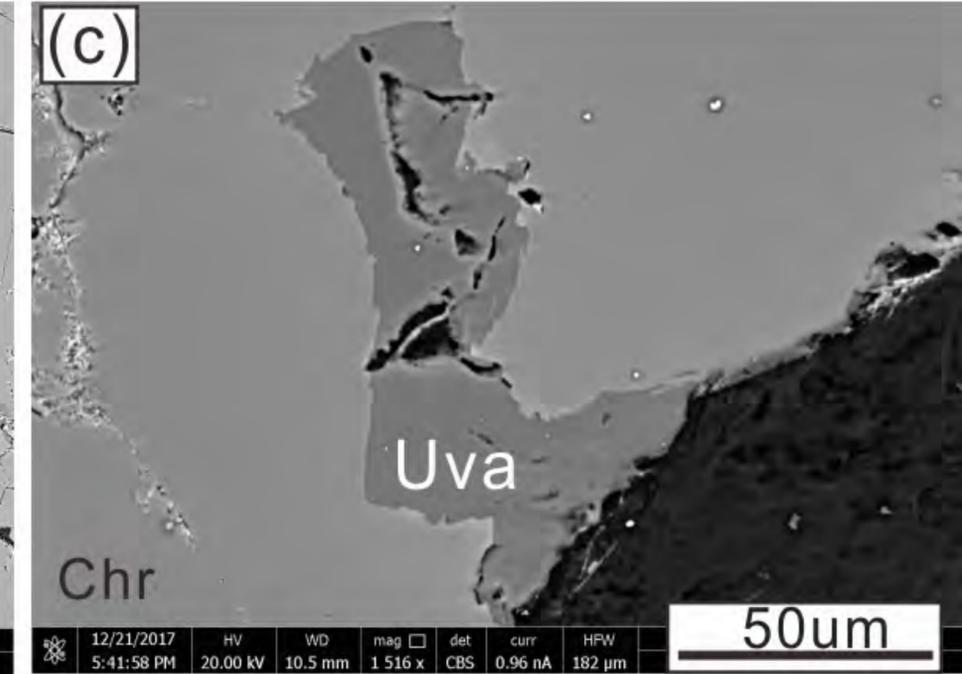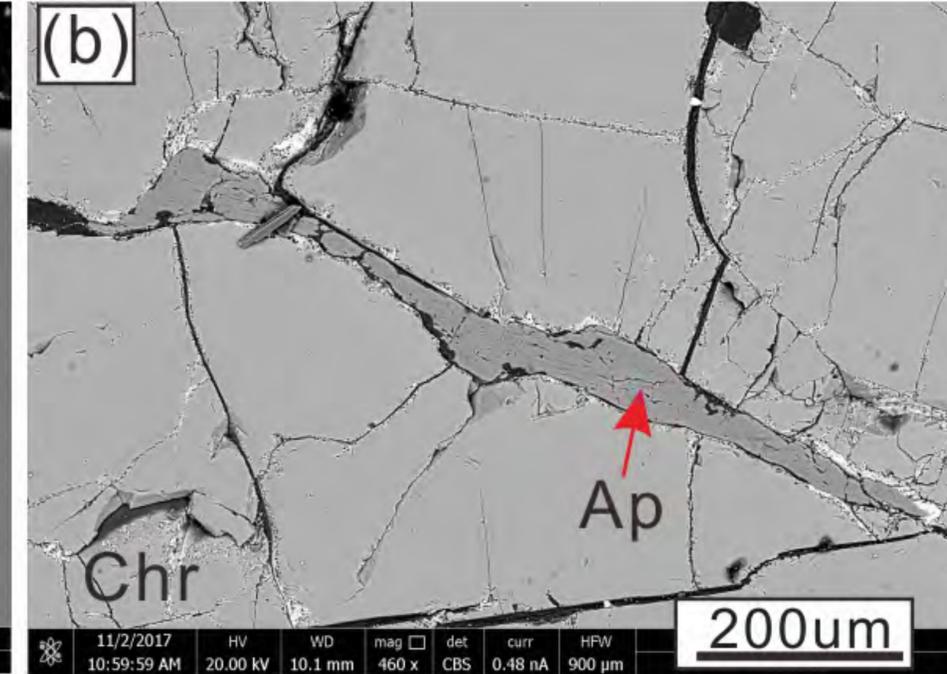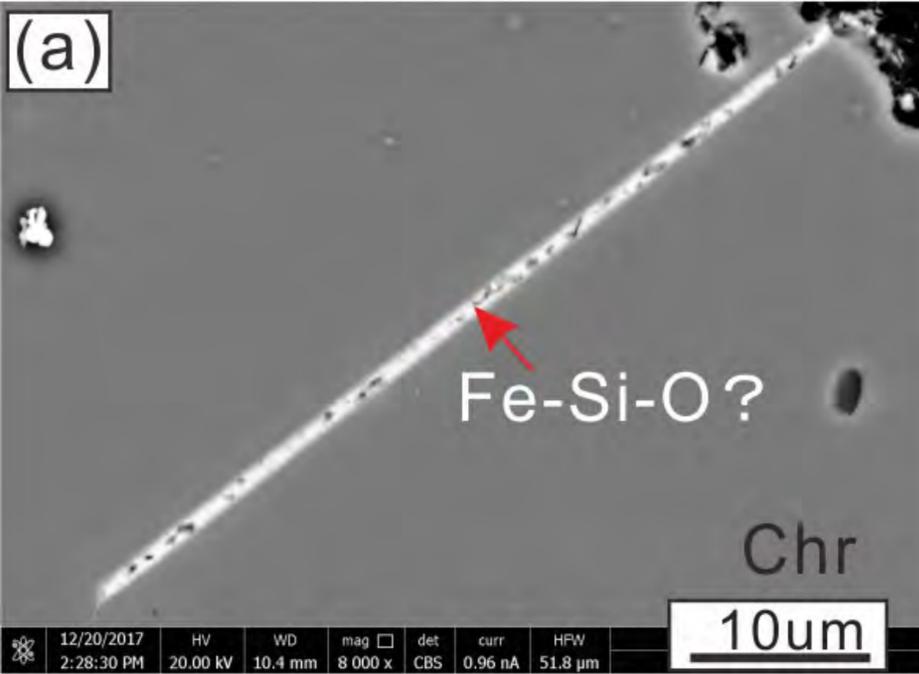
Figure 7
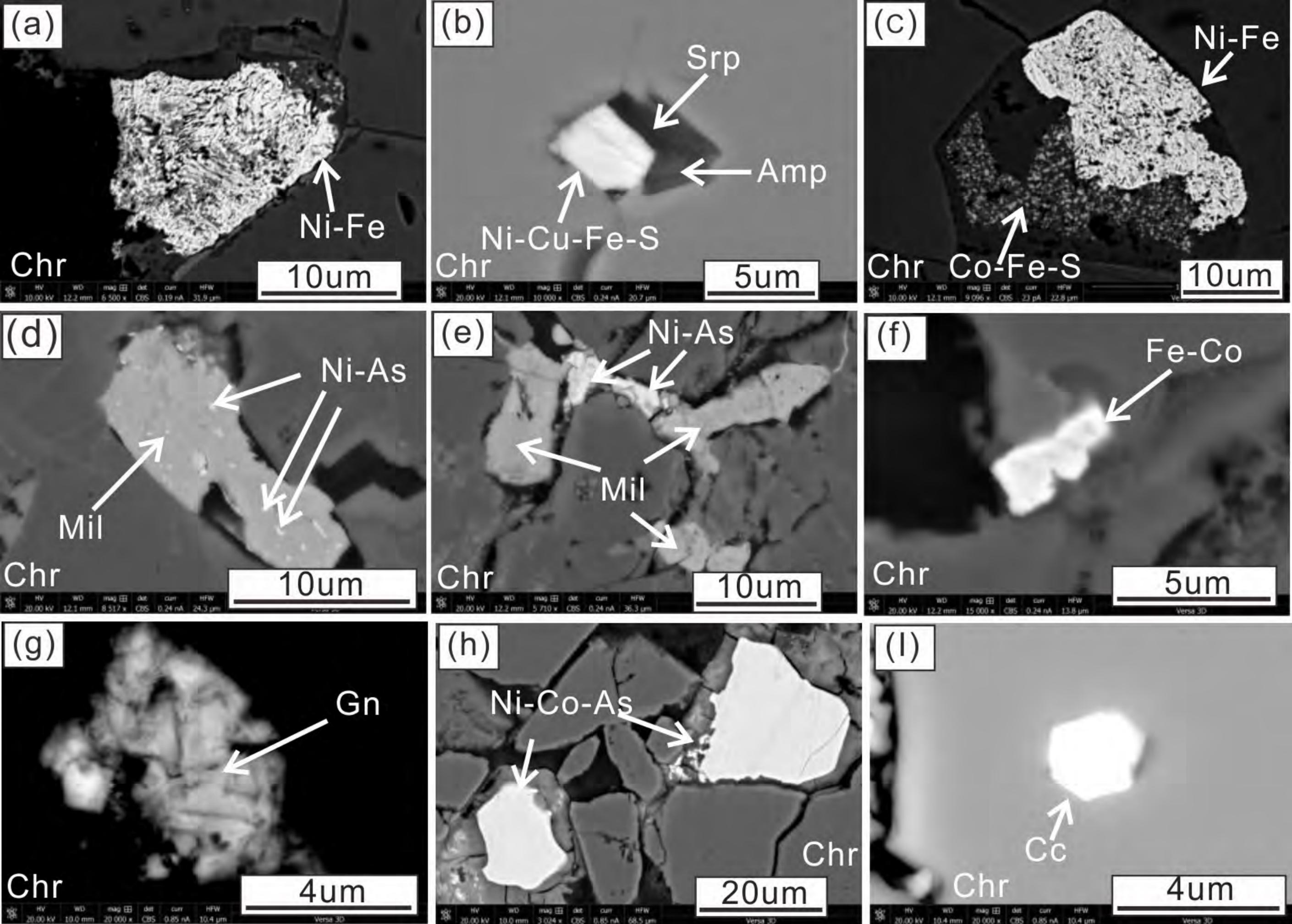
Figure 8
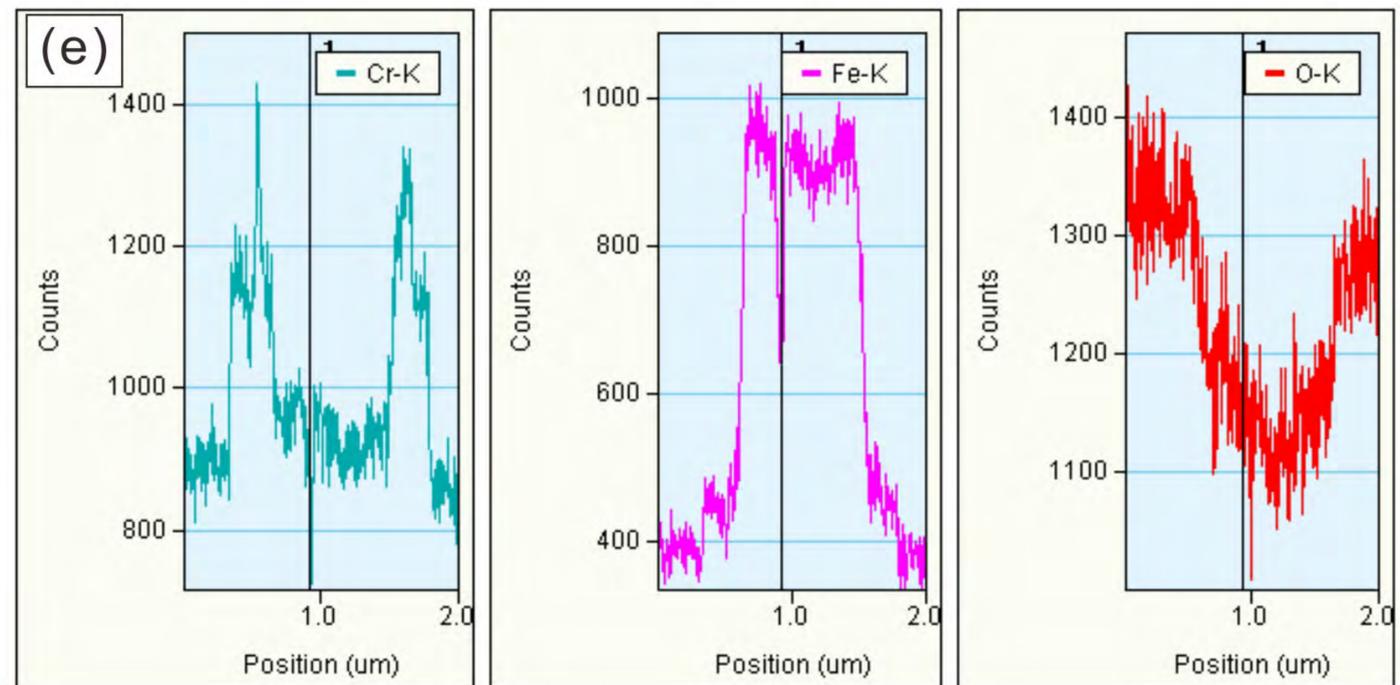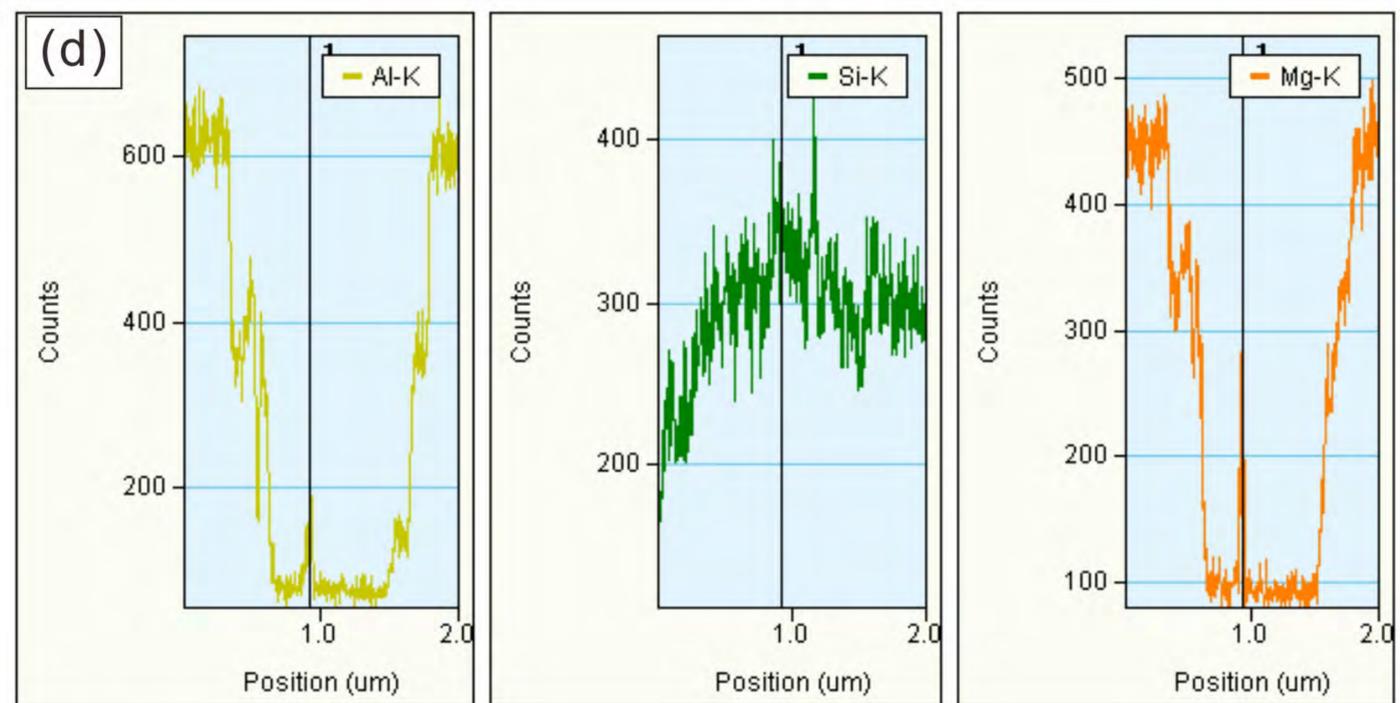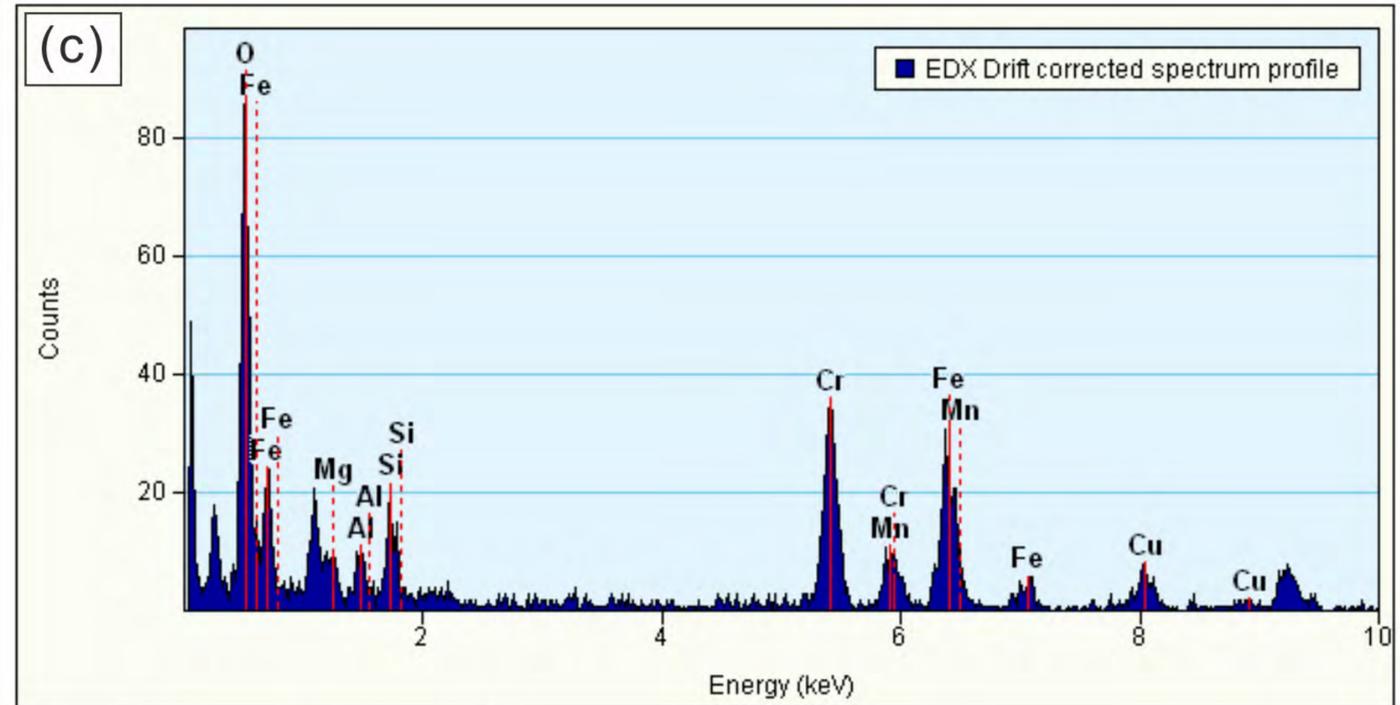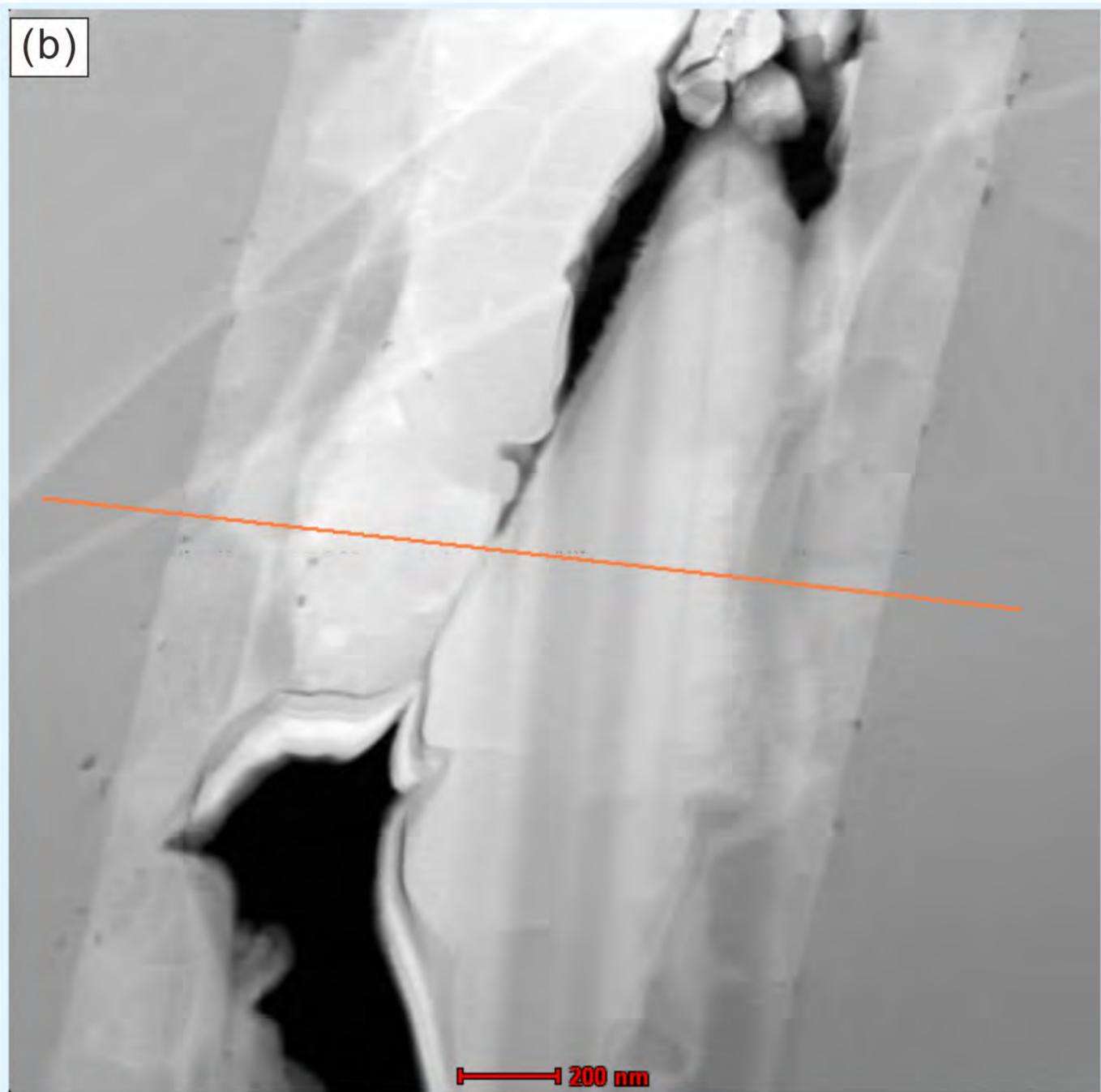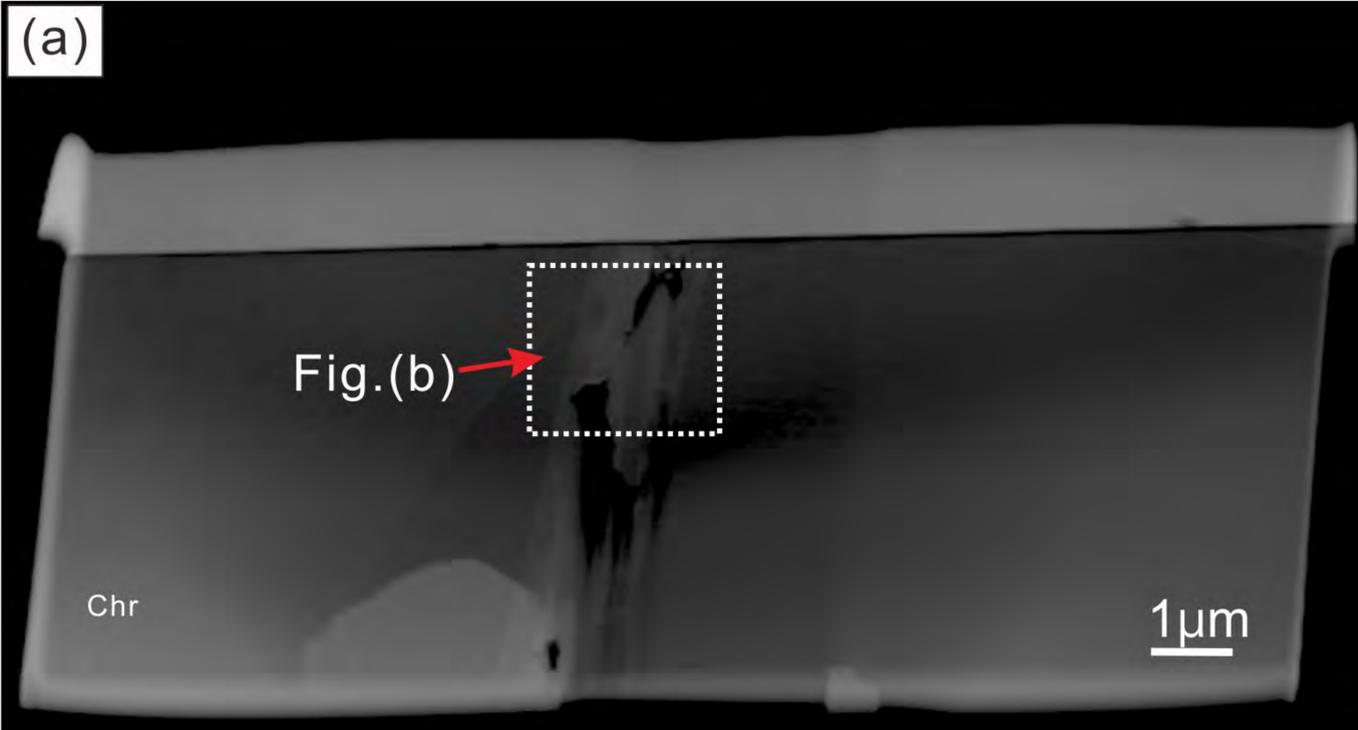
Figure 9
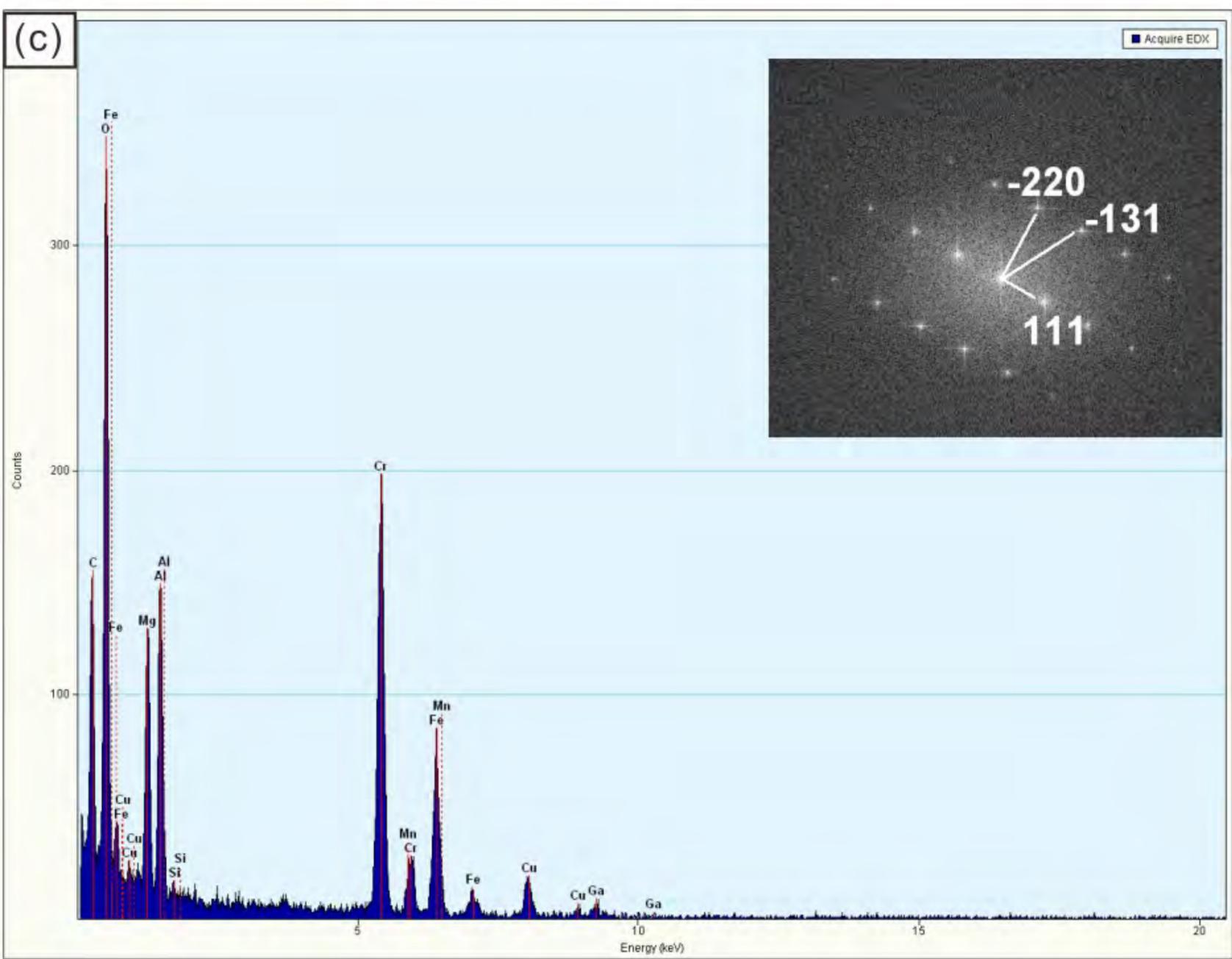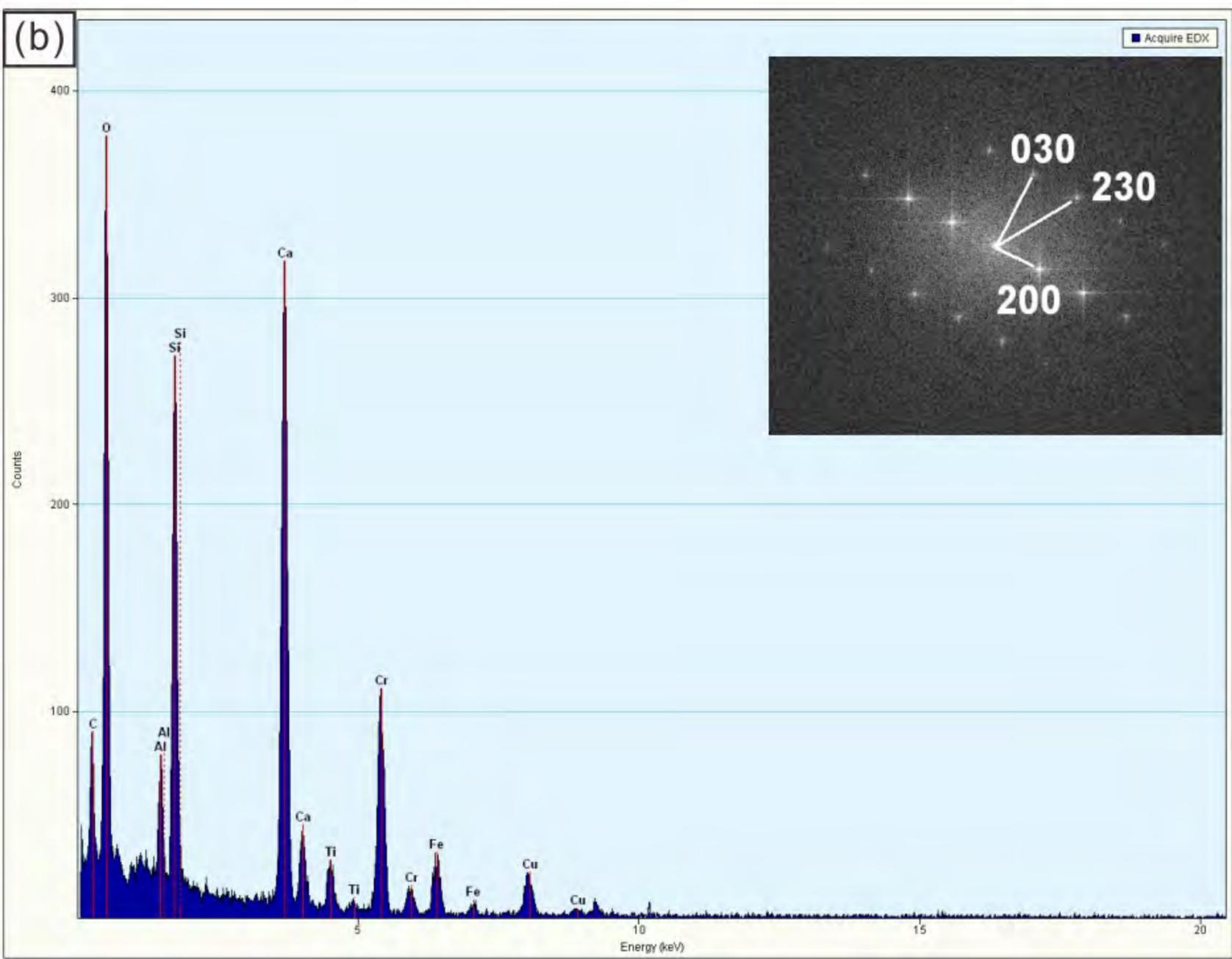
Figure 10
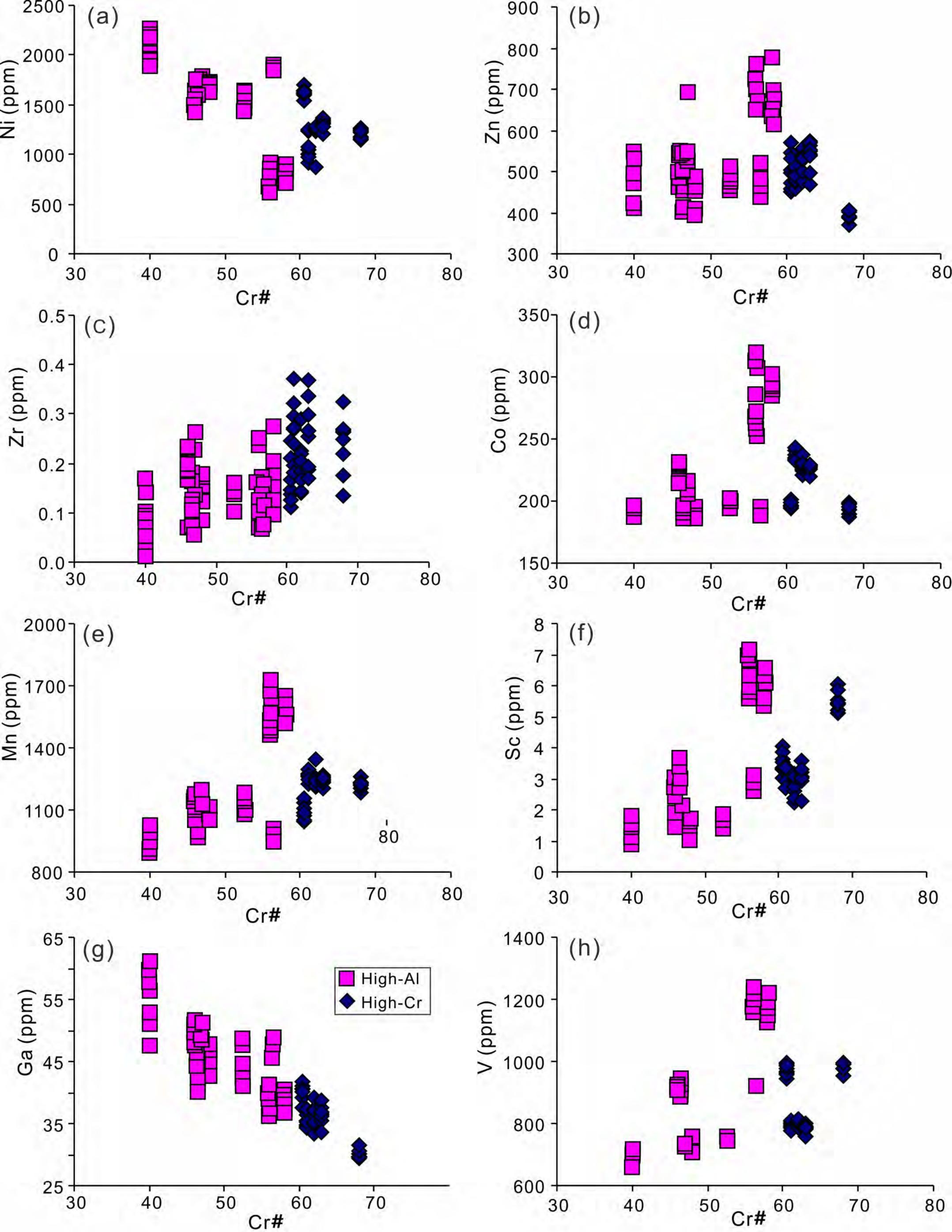
Figure 11
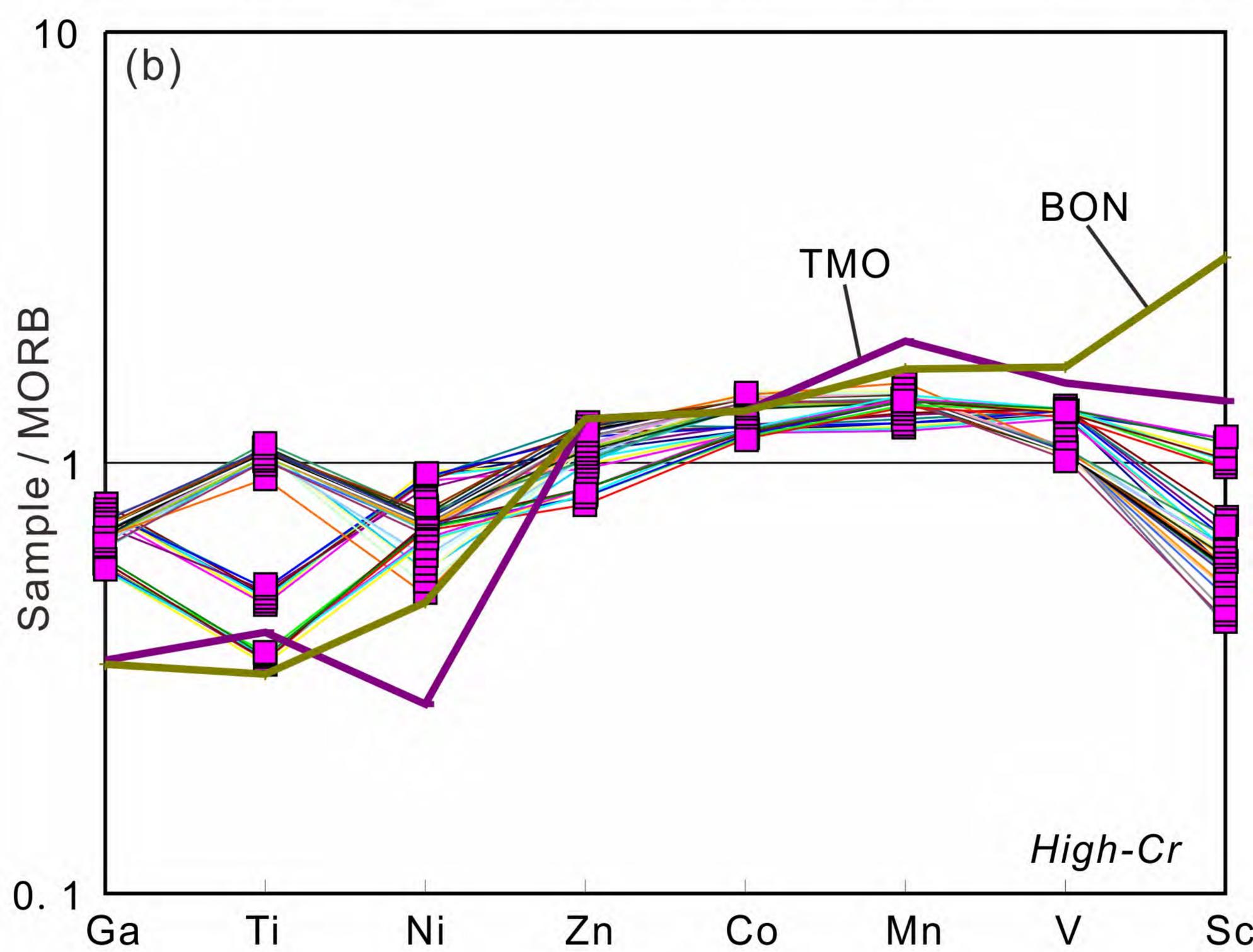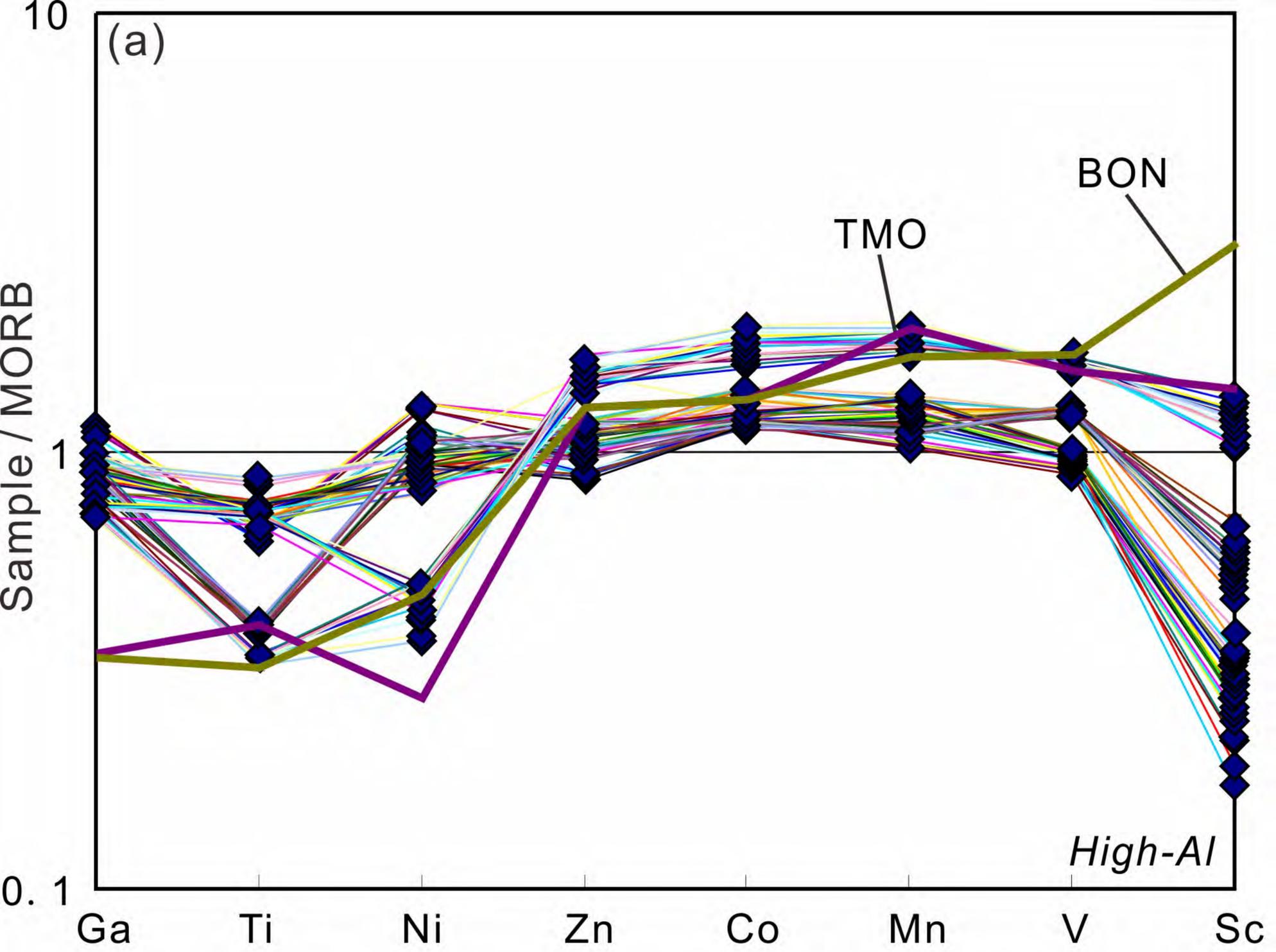
Figure 12
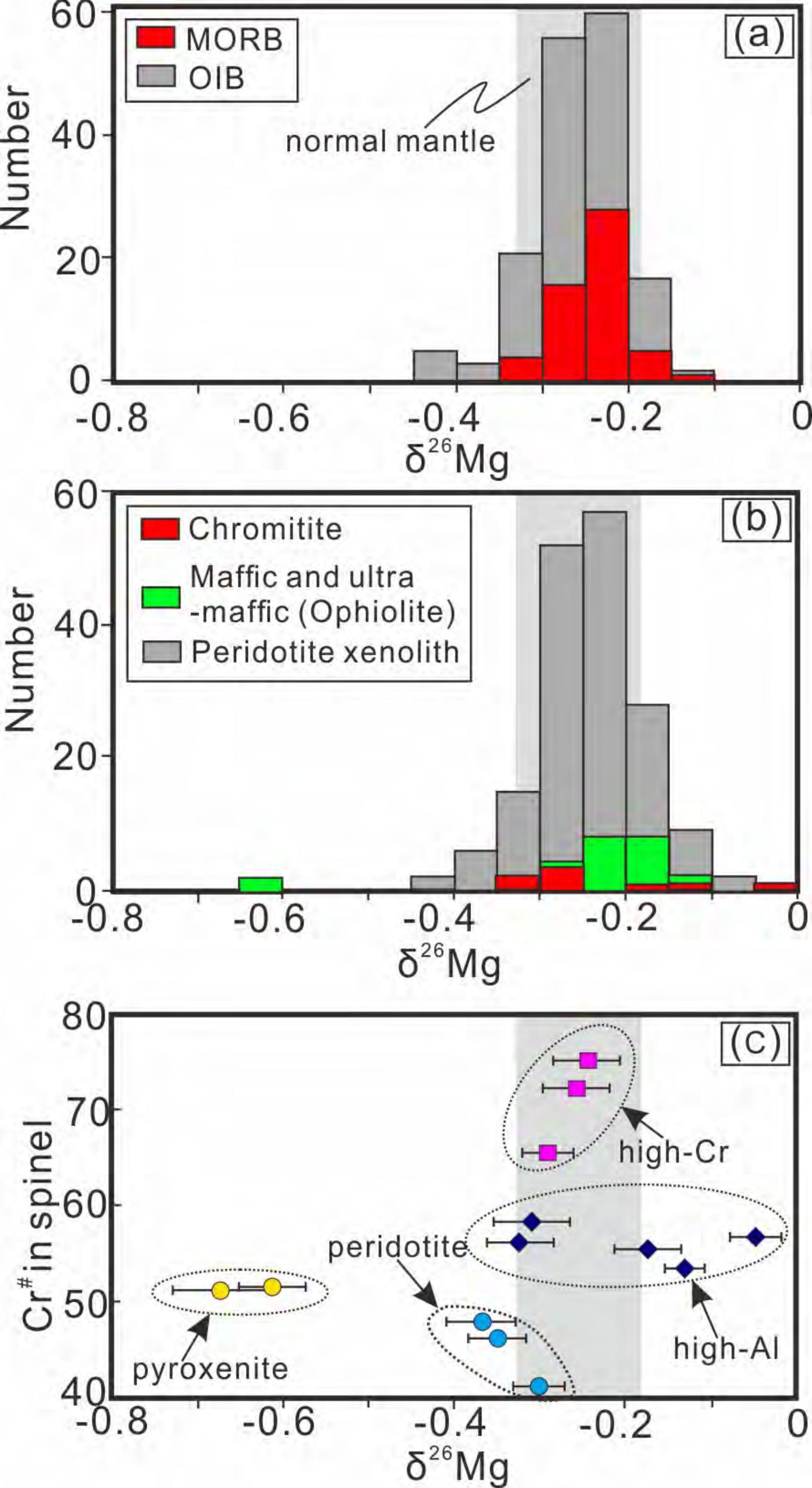
Figure 13

Table 1. Representative EPMA data of chromite grains from the Purang chromitites.

Lithology	High-Al chromitite					High-Cr chromitite					Harzburgite					Dunite				
Sample	17x.1	17x.2	17x.3	17x.4	17x.5	11Y-P214-2.1	11Y-P214-2.2	11Y-401-10.14	11Y-401-10.26	11Y-401-10.27	09y-636.1	09y-636.2	09y-636.3	09y-636.4	09y-636.5	1334c2-3	1334c2-7	1334c2-1	1334c2-1	1334c2-1
Cr_2O_3	42.24	42.59	43.29	43.04	42.92	64.17	64.46	54.50	55.14	54.86	34.268	33.67	35.005	33.698	34.941	38.889	37.681	38.76	37.255	38.228
Na_2O	0.02	0.00	0.02	0.02	0.01	0.01	0.01	0	0	0	0	0	0	0	0	0.03	0.01	0.00	0.00	0.03
K_2O	0.00	0.00	0.01	0.00	0.02	0.01	0.01	0.01	0.01	0.01	0	0	0	0.01	0.00	0.01	0.01	0.02	0.00	0.00
MgO	16.59	15.76	16.05	16.31	16.35	10.36	10.27	12.00	12.63	12.46	13.58	13.69	13.83	13.45	14.34	13.55	13.62	13.31	14.01	13.87
MnO	0.22	0.22	0.25	0.28	0.21	0.39	0.38	0.37	0.33	0.33	0.30	0.26	0.22	0.24	0.25	0.22	0.21	0.21	0.28	0.27
CaO	0.00	0.00	0.01	0.00	0.00	0	0	0	0	0	0.00	0.00	0.00	0.04	0.00	0.00	0.00	0.04	0.01	0.01
Al_2O_3	25.01	25.28	25.54	24.49	26.05	5.92	5.78	13.88	14.42	14.09	33.11	33.40	32.10	33.55	32.81	29.38	29.96	29.88	30.89	30.18
FeO	14.78	15.28	14.23	14.78	14.02	19.63	19.65	18.61	17.65	18.09	19.02	18.95	19.16	19.35	17.99	17.78	18.08	18.14	17.55	17.59
TiO_2	0.22	0.20	0.30	0.26	0.25	0.06	0.10	0.07	0.08	0.08	0.10	0.09	0.13	0.09	0.09	0.04	0.04	0.07	0.04	0.00
SiO_2	0.04	0.04	0.02	0.02	0.04	0	0	0	0	0	0.00	0.01	0.04	0.00	0.00	0.02	0.01	0.06	0.08	0.01
NiO	0.20	0.13	0.14	0.14	0.13	0.10	0.06	0.24	0.32	0.25	0.13	0.11	0.14	0.12	0.15	0.05	0.13	0.11	0.08	0.07
Total	99.32	99.49	99.84	99.33	99.99	100.63	100.69	99.68	100.58	100.16	100.50	100.18	100.61	100.55	100.57	99.97	99.75	100.59	100.20	100.25
Mg#	67.30	65.33	67.43	66.83	68.22	51.75	51.24	57.92	60.16	59.61	59.39	59.89	60.43	58.72	62.46	60.33	60.65	59.03	61.87	61.41
Cr#	53.12	53.06	53.21	54.11	52.50	87.91	88.20	72.47	71.94	72.30	40.97	40.34	42.24	40.25	41.66	47.02	45.76	46.52	44.71	45.93

Cr# =[100 x Cr^{3+}/(Cr + Al+Fe^{3+})]; Mg#=[100 x Mg/(Mg + Fe^{2+})]

Table 2. Representative EPMA data of silicate inclusions in chromite grains from the Purang chromitites (wt.%).

Minerals	Cpx	Cpx	Cpx	Cpx	Cpx	Opx	Opx	Opx	Opx	Opx
Sample	706.1	706.4	706.7	706.8	706.9	706.1	706.1	706.1	706.2	706.2
SiO_2	54.36	55.21	54.22	55.34	55.24	57.54	57.75	57.58	57.29	57.59
Na_2O	0.15	0.18	0.16	0.13	0.17	0.08	0.02	0.03	0.02	0.02
Cr_2O_3	1.03	0.83	0.84	0.95	0.99	0.92	0.86	0.87	0.79	0.91
K_2O	0.00	0.01	0.01	0.00	0.01	0.00	0.01	0.01	0.00	0.00
MgO	18.53	18.96	18.57	18.78	18.62	38.72	38.54	38.19	38.85	38.76
Al_2O_3	0.66	0.65	0.69	0.72	0.82	0.29	0.32	0.35	0.28	0.36
MnO	0.04	0.06	0.04	0.05	0.02	0.06	0.07	0.05	0.06	0.07
CaO	23.53	23.72	23.32	22.36	23.14	0.35	0.29	0.27	0.33	0.37
FeO	1.02	1.05	0.86	0.98	1.01	2.59	2.45	2.27	2.52	2.39
TiO_2	0.05	0.08	0.06	0.08	0.08	0.01	0.03	0.04	0.01	0.03
NiO	0.09	0.06	0.05	0.09	0.07	0.10	0.11	0.10	0.09	0.13
Total	99.46	100.81	98.82	99.48	100.17	100.66	100.46	99.76	100.24	100.63
En	51.5	51.8	51.9	53.1	52.0	95.8	96.1	96.3	95.9	96.0
Fs	1.6	1.6	1.3	1.6	1.6	3.6	3.4	3.2	3.5	3.3
Wo	47.0	46.6	46.8	45.4	46.4	0.6	0.5	0.5	0.6	0.7
Mg#	97.00	96.99	97.47	97.16	97.05	96.38	96.56	96.77	96.49	96.66

Mg#= [100 x Mg/(Mg + Fe^{2+})]

Table 3 Trace element composition, by LA-ICP-MS, of chromite grains from the Purang chromitites (ppm).

Sample	Lithos	FeO	MgO$_2$	Al$_2$O$_3$	SiO$_2$	TiO$_2$	MnO$_2$	Ga	Ti	Ni	Zn	Co	Mn	V	Sc	Cu	Zr	Nb	Cr	Cr#
662-16-1		11.87175196	185517	376065	4146	1407	1180	60	844	2260	531	191	914	689	1.7	3.8	0.14	0.11	208112	40
662-16-2		12.06163111	184904	375313	3741	1456	1203	58	874	2264	547	197	932	686	1.4	2.7	0.08	0.10	207638	40
662-16-3		11.82373195	186570	377186	4377	1478	1175	61	887	2272	531	189	910	681	1.3	0.6	0.07	0.13	206534	40
662-16-4		11.73283143	184180	378867	4500	1395	1165	56	837	2199	472	190	903	671	1.3	2.6	0.10	0.10	208376	40
662-16-5		11.64341467	187147	378294	7693	1467	1164	58	880	2187	472	189	902	669	1.5	1.8	0.02	0.07	204982	40
662-16-6		11.77160677	186447	379299	4224	1390	1161	60	834	2209	494	189	900	661	1.2	2.5	0.09	0.12	206635	40
692-6-1		12.28386142	183765	345077	1362	1403	1283	53	842	2020	416	196	994	705	1.2	0.1	0.05	0.06	209674	40
692-6-2		12.297554	184009	342277	2639	1404	1319	53	842	1957	415	194	1021	717	1.4	1.9	0.17	0.15	223616	40
692-6-3		12.20916705	185045	346267	1187	1487	1249	47	892	1895	412	188	968	709	0.9	1.7	0.09	0.16	224503	40
692-6-4		12.20725928	182415	345836	2408	1486	1279	51	892	1948	418	187	991	698	1.4	2.1	0.01	0.15	230407	40
662-27-1		13.14496029	173853	310537	3129	1892	1458	49	1135	1751	549	208	1129	724	1.6	1.1	0.11	0.12	252128	47
662-27-2		13.22578374	171278	309658	3341	1897	1552	51	1138	1771	694	210	1203	728	1.8	11.4	0.26	0.16	253023	47
662-27-4		13.33597043	172077	306745	3551	1936	1394	49	1161	1710	521	216	1080	734	1.6	0.0	0.23	0.11	234853	47
662-27-5		13.17331678	172996	309402	2021	1861	1384	48	1116	1715	486	209	1072	735	2.1	1.4	0.14	0.16	254928	47
662-27-6		13.17521911	173234	305668	2047	1892	1379	48	1135	1722	532	205	1068	731	1.8	0.6	0.06	0.16	254513	47
706-8-1		14.18433838	162602	315281	2915	1561	1520	51	937	1403	538	231	1178	909	2.9	1.2	0.07	0.16	257149	46
706-8-2		14.04933629	165080	311212	2429	1542	1495	49	925	1416	542	230	1158	906	2.9	1.8	0.20	0.14	251506	46
706-8-3		13.86847647	163429	315712	2533	1560	1475	51	936	1500	548	228	1142	921	3.0	1.9	0.23	0.11	250917	46
706-8-4		13.62209204	161450	309602	2430	1512	1434	50	907	1496	544	227	1111	905	2.8	1.8	0.23	0.14	258437	46
706-8-5		13.20825055	165671	312026	1912	1568	1382	47	941	1624	500	216	1070	923	1.4	1.8	0.19	0.16	257341	46
706-8-6		13.15610487	170370	317948	1885	1563	1361	48	938	1572	462	217	1054	915	1.9	0.8	0.18	0.17	250175	46
706-8-7		13.29751238	164898	314522	2418	1571	1419	48	942	1554	486	229	1099	925	2.4	1.5	0.17	0.15	255485	46
599-6-1-1		12.52587291	177158	291378	1746	856	1276	46	513	1754	504	196	988	893	3.2	2.5	0.12	0.21	268881	46.5
599-6-1-2		12.5112249	177041	290720	2526	859	1313	44	516	1725	480	192	1017	946	2.8	0.2	0.07	0.15	269298	46.5
599-6-1-3		12.57593438	174582	291879	2810	861	1256	44	516	1741	478	194	973	894	2.8	0.8	0.12	0.08	268879	46.5
599-6-1-4		12.61613136	176414	291077	3183	853	1282	45	512	1754	544	193	993	899	3.2	0.1	0.10	0.17	267816	46.5
599-6-1-5		12.62485704	174923	291642	2688	846	1287	46	507	1748	501	194	997	888	3.0	0.6	0.16	0.12	268915	46.5
599-6-1-6		12.75505568	172567	287671	2448	878	1324	42	527	1605	405	189	1026	931	3.4	1.5	0.18	0.14	272702	46.5
599-6-1-7		12.68073527	173363	288006	2709	880	1317	40	528	1640	412	191	1020	910	3.7	0.0	0.12	0.24	271754	46.5
599-6-1-8		12.26943341	168950	286788	2323	860	1247	41	516	1652	450	186	966	894	3.4	1.9	0.11	0.16	279175	46.5
662-4-1		12.67524986	169798	304735	2844	1623	1358	45	974	1607	409	186	1052	710	1.6	1.9	0.09	0.10	263166	48
662-4-2		12.72158359	173660	306595	2447	1614	1366	43	969	1647	400	189	1058	708	1.4	1.6	0.14	0.13	259042	48
662-4-3		13.0321589	169767	307439	4892	1750	1438	48	1050	1678	491	195	1114	752	1.7	0.9	0.14	0.13	255579	48
662-4-4		12.75604852	172100	311654	2334	1714	1371	45	1028	1622	455	194	1062	738	1.0	1.7	0.18	0.13	256614	48
662-4-5	High-Al chromitite	12.74996509	172522	311394	2687	1660	1367	48	996	1708	472	193	1059	734	1.5	0.8	0.12	0.15	255950	48
662-4-6		12.92407457	172057	313387	2893	1620	1385	47	972	1727	473	194	1073	742	1.6	1.1	0.15	0.18	253346	48
662-4-7		13.04575884	173075	311212	2273	1652	1392	46	991	1715	487	193	1079	729	1.5	1.1	0.12	0.22	254286	48
662-15-1		13.14250613	174419	289762	3189	1641	1413	42	984	1473	457	199	1094	743	1.8	0.2	0.14	0.12	266576	52.5
662-15-2		13.2672357	168471	289202	3912	1626	1483	41	976	1476	473	202	1149	755	1.8	2.1	0.16	0.10	268493	52.5
662-15-3		12.9922109	174750	307966	3844	1650	1473	48	990	1647	512	202	1141	752	1.4	1.9	0.16	0.14	254182	52.5
662-15-4		13.01864086	173910	313187	2070	1689	1396	47	1014	1633	481	201	1082	757	1.4	0.9	0.14	0.16	252793	52.5
662-15-5		13.27869982	171363	290352	2494	1687	1493	44	1012	1530	506	201	1157	757	1.7	2.5	0.10	0.11	268248	52.5
662-15-6		13.32887157	166656	277784	3310	1719	1526	42	1031	1478	509	195	1182	754	1.7	1.8	0.14	0.18	277727	52.5
599-5-1-1		12.49600684	178537	317624	2800	886	1231	48	531	1904	450	191	954	923	3.0	0.9	0.17	0.11	249871	56.5
599-5-1-2		12.28634768	179427	319179	2514	897	1227	49	538	1907	470	192	950	922	2.9	0.8	0.16	0.08	249575	56.5
599-5-1-3		12.46630614	176911	313628	2885	881	1253	46	529	1883	483	192	970	921	2.9	0.7	0.07	0.10	253721	56.5
599-5-1-4		12.41842237	184569	309754	2533	887	1229	46	532	1849	442	190	952	925	2.6	1.8	0.14	0.16	251753	56.5
599-5-1-5		12.41031731	175938	314429	2625	913	1263	46	548	1869	466	189	979	928	2.6	2.8	0.11	0.11	253867	56.5
599-5-1-6		12.63668083	178431	304129	2643	871	1300	48	523	1853	520	194	1007	924	3.1	2.0	0.07	0.13	257805	56.5
11YP-19-2-b1-Cr-1		17.11025849	150856	232337	2326	1615	1979	39	969	898	620	296	1533	1142	6.6	5.1	0.14	0.14	293758	58
11YP-19-2-b1-Cr-2		17.55184859	150650	229441	2133	1567	2038	39	940	884	619	294	1579	1163	6.5	1.5	0.25	0.14	292964	58
11YP-19-2-b1-Cr-3		17.57630239	147236	229938	1717	1582	2009	40	949	876	639	286	1557	1154	6.4	2.1	0.14	0.19	295242	58
11YP-19-2-b1-Cr-4		17.9246085	139984	235835	1723	1609	1978	39	965	820	681	293	1532	1130	6.2	1.6	0.11	0.17	293521	58
11YP-19-2-b1-Cr-5		17.8811418	139644	231960	1734	1658	2123	40	995	823	655	297	1644	1161	6.6	2.0	0.15	0.16	296633	58
11YP-19-2-b1-Cr-6		17.57451136	142499	235619	3433	1602	2052	39	961	796	671	297	1589	1181	6.3	3.8	0.17	0.16	293403	58
11YP-19-2-b1-Cr-7		17.63907244	138853	232425	1644	1577	2068	40	946	838	696	292	1602	1146	6.6	6.4	0.21	0.16	298961	58
11YP-19-2-b1-Cr-8		17.16028838	140796	241529	1793	1510	2020	37	906	754	776	294	1565	1209	5.4	1.5	0.12	0.18	294242	58
11YP-19-2-b1-Cr-9		17.67636666	139247	239860	1541	1653	2125	40	992	788	696	303	1646	1194	6.6	1.4	0.30	0.22	293252	58
11YP-19-2-b1-Cr-10		17.35752045	139423	238432	2007	1659	2055	39	995	802	652	294	1592	1178	5.6	1.6	0.27	0.21	296122	58
11YP-19-2-a2-Cr-1		17.01260236	144184	242280	1591	771	1933	39	463	831	725	267	1497	1227	7.1	1.6	0.19	0.10	292854	56
11YP-19-2-a2-Cr-2		17.00316694	145564	241771	2423	755	1957	41	453	903	689	270	1516	1222	7.1	1.6	0.18	0.10	291597	56
11YP-19-2-a2-Cr-3		16.97904728	147964	240252	2418	761	1933	39	457	901	656	259	1497	1224	7.2	2.4	0.37	0.22	291516	56
11YP-19-2-a2-Cr-4		17.8240375	154482	234820	2159	769	1894	37	461	829	661	253	1467	1203	6.9	2.2	0.24	0.17	285485	56
11YP-19-2-a2-Cr-5		18.00615694	145964	236327	1721	746	2011	38	448	784	702	287	1558	1212	5.6	0.7	0.27	0.17	289085	56
11YP-19-2-a2-Cr-6		18.98331062	141471	235333	2021	761	2128	38	456	730	703	308	1649	1207	6.1	1.1	0.32	0.16	285819	56
11YP-19-2-a2-Cr-7		17.60441253	154689	234785	2096	739	1940	38	444	882	727	270	1502	1187	6.0	2.3	0.18	0.16	286628	56
11YP-19-2-a2-Cr-8		19.41557788	142093	226618	1911	745	2234	37	447	669	756	318	1730	1181	7.1	0.0	0.29	0.19	287980	56
11YP-19-2-a2-Cr-9		19.40570221	142013	238444	2106	725	2179	40	435	652	760	314	1688	1180	6.3	1.6	0.22	0.15	280070	56
11YP-19-2-a2-Cr-10		17.96530047	157013	231859	2067	757	1994	38	454	879	674	273	1545	1167	6.0	2.1	0.22	0.16	284567	56
599-2-1-1		14.22213954	165388	256089	3216	1094	1404	41	657	1636	495	196	1088	962	3.0	1.0	0.14	0.15	286383	60.5
599-2-1-2		13.21621033	163750	267413	2517	1049	1347	39	629	1600	452	194	1043	942	3.3	0.4	0.14	0.15	287614	60.5
599-2-1-3		13.31834166	167899	264447	2067	1063	1382	41	638	1694	458	196	1071	966	3.3	0.5	0.20	0.16	287108	60.5
599-2-1-4		13.32230868	168149	259875	2885	1088	1359	41	653	1644	473	195	1053	960	3.4	0.5	0.17	0.17	289069	60.5
599-2-1-5		13.6842958	162540	238873	2432	1130	1469	37	678	1537	502	201	1138	989	3.6	0.9	0.34	0.12	304568	60.5
599-2-1-6		13.72154	163586	246022	3387	1102	1492	42	661	1607	545	201	1156	994	4.0	0.4	0.53	0.16	298254	60.5
599-2-1-7		13.42007311	161182	244193	8271	1144	1433	41	686	1616	571	199	1110	979	3.9	1.7	0.37	0.17	295924	60.5
599-2-1-9		13.33068922	166988	249322	3967	1142	1404	40	685	1634	532	199	1088	985	3.5	0.9	0.19	0.16	290238	60.5
567-4-1-2		14.11001881	154406	223120	2829	2402	1640	35	1441	996	459	240	1270	793	3.4	1.6	0.19	0.19	318726	61
567-4-1-3		14.65016041	155444	214480	3291	2357	1646	36	1414	1044	475	243	1275	800	3.3	1.9	0.17	0.14	319603	61
567-4-1-4		14.68429436	153690	225101	2052	2352	1644	35	1411	914	500	237	1274	787	3.2	1.2	0.25	0.18	314064	61
567-4-1-5		13.89802395	155461	221632	1980	2367	1673	35	1420	980	505	243	1296	792	3.3	1.1	0.27	0.19	321060	61
567-4-1-6		13.91404475	159047	218781	1984	2307	1630	34	1384	1076	480	234	1263	806	3.3	0.2	0.30	0.15	320555	61
567-4-1-7		14.04127595	156501	222666	2156	2386	1641	37	1432	1240	506	234	1271	808	3.0	1.8	0.32	0.17	318157	61
567-4-1-8		13.82870678	154599	219684	6240	2366	1586	35	1420	1243	511	235	1228	788	3.4	1.7	0.27	0.20	317872	61
567-4-1-9		14.06408073	157452	224220	2208	2341	1613	37	1405	1255	488	232	1249	777	2.7	0.7	0.17	0.17	316236	61
567-3-Cr-1		13.60091825	160046	219964	2562	2262	1563	35	1357	1238	475	225	1211	798	2.6	0.7	0.26	0.20	321381	62
567-3-Cr-2		13.62884545	163220	219201	4416	2343	1589	33	1406	1229	475	221	1231	794	3.0	0.6	0.27	0.20	316480	62
567-3-Cr-3		13.59607529	163304	218770	2573	2309	1573	35	1386	1263	502	226	1219	788	3.0	1.3	0.14	0.15	319932	62
567-3-Cr-4		13.812307	162274	217801	2225	2378	1616	37	1427	1257	534	228	1252	803	3.2	0.7	0.22	0.16	319928	62
567-3-Cr-5	High-Cr chromitite	13.99003037	161812	220715	2015	2326	1596	36	1396	1247	529	232	1237	805	2.7	0.7	0.25	0.16	317286	62
567-3-Cr-7		14.41951006	157798	217562	2326	2051	1740	35	1231	871	555	238	1348	800	3.1	1.1	0.10	0.17	314150	62
567-3-Cr-8		13.67926873	164203	223288	1660	2345	1573	37	1407	1265	534	230	1219	807	2.2	0.5	0.15	0.12	318948	62
567-3-Cr-9		13.82523631	165607	222971	1621	2336	1598	39	1402	1276	531	230	1238	812	2.4	0.0	0.13	0.18	316302	62
567-3-2-1		13.45257666	158334	221224	4117	2388	1602	37	1433	1316	563	226	1241	782	3.1	0.5	0.13	0.18	314270	63
567-3-2-2		13.80667921	159848	221344	2675	2499	1595	37	1499	1355	468	220	1236	802	3.6	1.0	0.21	0.18	317712	63
567-3-2-3		13.44110465	157979	219996	1661	2433	1558	35	1460	1312	497	220	1207	786	3.0	0.8	0.27	0.14	323880	63
567-3-2-4		13.69116196	161350	220895	3798	2400	1638	37	1440	1340	575	229	1269	785	3.2	1.0	0.16	0.14	317345	63
567-3-2-5		13.54849368	162811	228330	2114	2385	1560	38	1431	1368	570	229	1208	790	3.1	0.8	0.15	0.14	313795	63
567-3-2-6		13.49186925	159921	214301	1768	2254	1590	34	1353	1202	541	227	1231	758	2.3	1.2	0.18	0.11	326839	63
567-3-2-7		13.87662006	160337	221572	2139	2404	1613	39	1443	1302	548	229	1250	792	2.9	0.0	0.21	0.19	318114	63
567-3-2-8		13.74428484	163342	220784	1836	2370	1623	36	1422	1284	552	229	1258	786	3.0	0.6	0.14	0.19	318042	63
567-3-2-9		13.89725933	159746	221949	1745	2345	1615	37	1407	1284	539	229	1251	786	3.3	2.0	0.24	0.20	318361	63
L-43-2-1		13.61647586	159919	191418	3456	780	1527	30	468	1226	371	187	1183	953	5.1	1.9	0.13	0.23	342721	68
L-43-2-2		13.82824954	160583	195825	4979	810	1557	30	486	1240	387	190	1206	977	5.2	2.1	0.10	0.15	336741	68
L-43-2-3		13.88084006	160847	195119	3523	789	1588	30	474	1252	388	193	1230	975	6.0	3.1	0.13	0.11	337622	68
L-43-2-4		13.95446439	160815	192189	3517	761	1575	30	457	1149	407	198	1220	977	5.5	0.8	0.16	0.15	339652	68
L-43-2-5		14.00547652	161969	191591	4447	799	1595	30	479	1181	403	199	1236	995	6.1	5.0	0.10	0.13	338100	68
L-43-2-6		13.7739476	161404	197580	3562	793	1626	30	476	1167	391	198	1260	989	5.4	1.1	0.25	0.14	336251	68
L-43-2-7		13.87128015	161016	193176	3799	778	1591	31	467	1267	407	193	1232	976	5.4	1.5	0.07	0.12	338646	68
L-43-2-8		13.88501446	161073	198480	2680	793	1586	32	476	1243	404	195	1229	997	5.9	4.1	0.13	0.18	335730	68

Table 4 Mg isotopic compositions of selected samples from the Purang chromitites and associated peridotites.

Sample Standard	Rock type	δ^{25}Mg	2SD	δ^{26}Mg	2SD	Cr# in spinel
GSB		-1.03	0.04	-2.01	0.03	
GSB		-1.05	0.04	-2.04	0.03	
BCR-2		-0.12	0.04	-0.25	0.03	
BHVO-2		-0.13	0.05	-0.27	0.04	
11YP-19-b2	high-Al chromitite	-0.16	0.03	-0.31	0.05	58.4
11YP-19-b1	high-Al chromitite	-0.15	0.02	-0.32	0.04	56.2
10y-22-3	high-Al chromitite	-0.08	0.05	-0.13	0.02	53.5
10y-22-b	high-Al chromitite	-0.09	0.03	-0.17	0.04	55.5
11YP-19-1	high-Al chromitite	-0.02	0.02	-0.05	0.03	56.9
11Y-401-1a	high-Cr chromitite	-0.12	0.01	-0.25	0.04	75.2
11Y-401-2	high-Cr chromitite	-0.14	0.03	-0.29	0.03	65.6
11Y-401-1b	high-Cr chromitite	-0.12	0.04	-0.26	0.04	72.3
B3R30P1	harzburgite	-0.13	0.03	-0.26	0.02	40.3
B14R665P1c	harzburgite	-0.19	0.05	-0.37	0.04	48.4
B25R82P3b	harzburgite	-0.17	0.05	-0.35	0.03	46.8
11YP-19-a2	pyroxenite	-0.31	0.02	-0.61	0.04	51.6
11YP-19-a1	pyroxenite	-0.33	0.07	-0.67	0.06	51.2

.

Sample Standard	Rock type	δ^{25}Mg	2SD	δ^{26}Mg	2SD	Cr# in spinel